JOURNAL OF GEOPHYSICAL RESEARCH, VOL. 88, NO. A6, PAGES 4813-4840, JUNE 1, 1983

THE APPARENT SPECTRAL BROADENING OF VLF TRANSMITTER SIGNALS DURING TRANSIONOSPHERIC PROPAGATION

T. F. Bell

STAR Laboratory, Stanford University, Stanford, California 94305

H. G. James

Communications Research Centre, Shirley Bay, Ottawa, Ontario, Canada K2H 8S2

U. S. Inan and J. P. Katsufrakis

STAR Laboratory, Stanford University, Stanford, California 94305

Abstract. VLF/ELF electric field wave data acquired on the ISIS 1, ISIS 2, and ISEE 1 satellites demonstrate the existence of a new phenomenon in which initially narrowband (~1 Hz) upgoing signals from ground-based VLF transmitters undergo a significant spectral broadening as they propagate through the ionosphere and protonosphere up to altitudes in the range 600-3800 km. For transmitter signals in the range 10-20 kHz, the spectral broadening can be as high as 10% of the nominal frequency of the input signal. Spectral broadening occurs only in the presence of impulsive VLF hiss and/or a lower hybrid resonance (LHR) noise band with an irregular lower cutoff frequency, and only for signals whose frequency exceeds the LHR frequency at the satellite location. It is often observed in association with a band of impulsive ELF hiss below 700 Hz. In many cases, the bandwidth of the spectrally broadened signals is a strong function of the electric dipole antenna orientation with respect to the local direction of the earth's magnetic field. Unusual dispersion in the components of the spectrally broadened pulses suggests that the spectral broadening may be due to a doppler shift effect in which the initial signals scatter from irregularities in the F region and couple into quasi-electrostatic modes of short wave length. The large doppler shift associated with these short wavelength modes produces a significant increase in the bandwidth of the signal, as observed on a moving satellite. Since impulsive VLF hiss and irregular LHR noise bands have been linked to energetic (<1 keV) electron precipitation in the past, it is conjectured that the spectral broadening effect may be driven by precipitating electrons.

1. Introduction

This paper presents satellite observations of a new phenomenon in which initially narrowband (~1 Hz) signals from ground-based VLF transmitters undergo a significant spectral broadening as they propagate through the ionosphere and protonosphere up to satellite altitudes in the range 600-3800 km. The transmitter signals lie in the range 10-20 kHz and the spectral broadening can reach as much as 10% of the nominal frequency of the input signals.

The spectral broadening effect occurs only in the presence of impulsive VLF hiss and/or a lower hybrid resonance (LHR) noise band with irregular lower cutoff frequency, and it is often associated with impulsive ELF hiss below 700 Hz. Spectral broadening occurs only for those transmitter signals whose frequency exceeds the local LHR frequency at the satellite location, and the bandwidth of these signals often shows a strong dependence upon the orientation of the dipole antenna with respect to the local direction of the earth's magnetic field.

All observations of this new phenomenon were carried out by VLF/ELF plasma wave experiments that used electric dipole antennas as wave detectors, and it is not presently known how the wave magnetic field is affected. The existence of the effect was first reported at meetings of the American Geophysical Union in December 1981 [Bell et al., 1981b] and May 1982 [Bell et al., 1982].

As discussed in section 2.3., we interpret the spectral broadening effect to be due to a doppler shift mechanism in which the transmitter signals are scattered from irregularities in the F region and couple into short wavelength quasi-electrostatic modes that are observed on the moving spacecraft with a large doppler shift. If our interpretation is correct, the observed spectral broadening does not represent a true spread in wave frequency but is instead an 'apparent' broadening, since to a stationary observer all scattered wave components would possess the same frequency.

The spectral broadening effect was discovered during joint VLF wave-injection experiments involving the Communications Research Centre at Ottawa, Canada, and the Stanford University Radioscience Laboratory. The joint wave-injection experiments have four main components: (1) broadband VLF/ELF receivers on the ISIS 1, ISIS 2, and ISEE 1 satellites, (2) a broadband (1-20 kHz) controllable VLF transmitter located at Siple Station, Antarctica [Helliwell and Katsufrakis, 1974], (3) various VLF navigation and communication transmitters, such as those of the worldwide Omega network, and (4) ground stations in the Antarctic and Canada.

The main goal of these, and similar, experiments is to acquire understanding of interactions between coherent VLF waves and energetic particles in the magnetosphere [Helliwell and Katsu-

Paper number 3A0139.
0148-0227/83/003A-0139$05.00

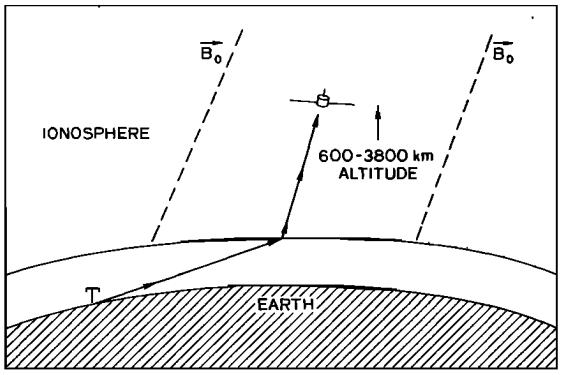

Fig. 1. Schematic representation showing a typical experimental configuration during periods in which spectral broadening of VLF transmitter signals was observed on satellites. Both transmitter and low-altitude satellite were in the northern hemisphere with the invariant latitude of the satellite lying in the range 45-80°N and the altitude of the satellite lying in the range 600-3800 km. Distance in the earth-ionosphere waveguide between transmitter (T) and subsatellite point lay in the range 300-3000 km.

frakis, 1974; McPherson et al., 1974; Dowden et al., 1978; Bell et al., 1981a]. Sources of the coherent waves involved in these studies include VLF transmitters, large-scale power grids, whistlers, and other natural coherent VLF signals.

The vital role of satellites in these studies is to obtain in situ measurements of the characteristics of the waves and energetic particles before, during and after the interactions. To this end, measurements by both low-altitude and high-altitude satellites are needed. Detailed results of ISEE 1 satellite high-altitude observations during wave-injection experiments can be found in the literature [Bell et al., 1981a]. In the present work we confine our attention to satellite measurements of the characteristics of VLF transmitter signals at low altitude (600-3800 km) before these signals enter the magnetosphere and interact significantly with the trapped energetic particle population of the magnetosphere. In this low-altitude region, as we show below, the VLF transmitter signals can develop a spectral broadening of up to 2 kHz about their nominal frequency.

This large spectral broadening is unlike the spectral broadening of VLF transmitter signals that occurs near the magnetic equatorial plane through the VLF emission triggering mechanism [Helliwell and Katsufrakis, 1974; Bell et al., 1981a]. However, it does bear some similarities to the doppler broadening reported previously by other workers that occurs in transmitter signals that have propagated through the magnetosphere into the conjugate hemisphere [Walter, 1969; Cerisier, 1974; Edgar, 1976b]. These similarities, as well as major differences, are discussed in section 3.8.

As depicted in Figure 1, the type of spectral broadening considered here occurs generally only in the ionosphere and low-altitude magnetosphere as VLF transmitter signals propagate upward along the short direct path (600-3800 km) to the satellite. This type of spectral broadening is apparently a new phenomenon which has not previously been treated in the literature. Its presence may demonstrate the existence of a new type of interaction involving energetic electrons and coherent VLF waves in the ionosphere and low-altitude magnetosphere.

In the following section we will be concerned primarily with signals from the 10 kW Omega navigation transmitter in North Dakota (46°22'N, 98°20'W geographic) and from the ~1 MW, 17.8 kHz, U.S. Navy Radio Station, NAA, in Maine (42°42'N, 67°18'W geographic). The 10-s format of the Omega North Dakota transmitter is shown in Figure 2. Since the oscillator frequency for the Omega North Dakota transmitter is stable to better than 1 part in 10^{11} the bandwidth of the Omega pulses is approximately equal to its intrinsic value, BW ~ (pulse length)$^{-1}$ ~ 1 Hz.

Signals from the NAA transmitter are transmitted in a 'minimum shift-keying' (MSK) format. This format generally consists of transmissions of 5-ms pulses at either of the two closely spaced frequencies, 17.8 kHz ± 50 Hz. MSK is a special case of frequency shift-keying (FSK) in which the sideband separation is equal to one-half of the information bit rate. Since the number of frequency shifts in any given time period depend upon the information to be transmitted, the MSK signal has a quasi-random nature. However, the apparent bandwidth of portions of the signal whose duration greatly exceeds the bit length (5 ms) is generally less than 200 Hz [Bruene, 1971].

The ISIS 1 spacecraft has an elliptical orbit (570 km perigee, 3520 km apogee) with 88° prograde inclination, while ISIS 2 is in a nearly circular orbit at approximately 1400 km altitude with an inclination of 89° prograde. The 75-m (tip-to-tip) receiving dipole antennas

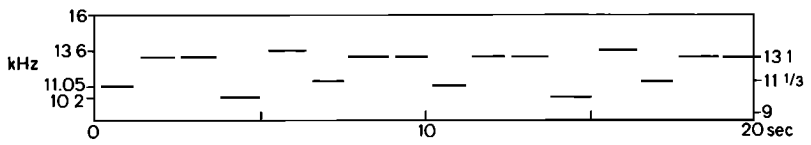

Fig. 2. Two cycles of the Omega North Dakota format. The basic cycle consists of eight fixed-frequency pulses distributed as follows: one pulse at 10.2 kHz with duration 1.1 s, one pulse at 11.3 kHz with duration 0.9 s, two pulses at 13.1 kHz with respective durations of 1.2 and 1.0 s, one pulse at 11.05 kHz with duration 0.9 s, and two pulses at 13.1 kHz with respective durations of 1.0 and 1.1 s. Each pulse is separated in time from its successor by 200 ms. The 10-s format is repeated continuously.

[Florida, 1969] and the VLF receivers [Franklin et al., 1960] are identical on the two spacecraft for present purposes. The receivers operate in the 50 Hz to 30 kHz range, featuring a linear amplifier with an automatic gain control (AGC) providing a total dynamic range of ~70 dB. Signals are telemetered to ground recording in real time using a conventional FM modulation scheme.

The ISEE 1 spacecraft is in a highly elliptical orbit (~1000 km perigee, 140,000 km apogee) of moderate inclination (30-50°) and ~2.5-day period. The Stanford University VLF receiver on ISEE 1 is connected to a 215-m dipole antenna and operates in the range 1-32 kHz [Bell and Helliwell, 1978]. It features a linear amplifier of ~30 dB dynamic range that can operate at any one of eight gain settings spaced equally over a 70 dB range. The gain state is updated every 5.4 s in order to deliver a signal of appropriate amplitude to the TLM system. Signals are telemetered to ground recording in real time using a conventional PM modulation scheme.

For purposes of the present work, we define the bandwidth of the observed transmitter signals to be the frequency difference between the points in the signal power spectral density curve which lie 10 dB below its peak value. Since the S/N ratio of the transmitter signals is typically ~20 dB (e.g., see Figure 11), the 10-dB points give a reliable measure of bandwidth. the 'dynamic range' of the gray scale of the photographic paper used to make the spectrograms is approximately 10 dB, and thus the 10-dB bandwidth definition ensures that the apparent bandwidth of signals shown in spectrograms will agree roughly with bandwidths determined from power density plots.

2. Observations

There are seven main characteristics of the phenomenon of the spectral broadening of VLF transmitter signals during transionospheric propagation (as observed on satellites with electric dipole antennas). We define these characteristics below and then follow with a discussion of each characteristic in turn:

1. Spectral broadening occurs only in the presence of impulsive VLF hiss and/or an LHR noise band with an irregular lower cutoff frequency.
2. Spectral broadening occurs only for those transmitter signals whose frequency exceeds the local LHR frequency at the satellite location.
3. The bandwidth of the spectrally broadened signals often shows a strong dependence upon the orientation angle of the dipole antenna with respect to the local direction of the earth's magnetic field, with the maximum bandwidth occuring when the dipole antenna is almost parallel to the ambient magnetic field.
4. The envelope of the spectrally broadened signals in amplitude-frequency-time displays generally has a characteristic 'chevron' shape in which the time delay of each spectral component at frequency f is an increasing function of the magnitude of the difference frequency between f and the nominal carrier frequency.
5. In many cases an amplitude minimum occurs within a few hertz of the nominal carrier frequency of the spectrally broadened signals.
6. Spectral broadening is often observed in association with a band of impulsive hiss below 700 Hz whose upper cutoff frequency strongly depends upon the orientation of the dipole antenna with respect to the local direction of the earth's magnetic field.
7. Spectral broadening is observed over a wide altitude range (600-3800 km) and a wide range of L shells ($2.3 < L < 11$) and appears to be a consistent feature associated with the propagation of coherent VLF waves through the ionosphere and lower magnetosphere.

2.1. Relation to Natural VLF Noise Bands

Figure 3 shows four spectrograms of VLF data acquired on the ISIS 2 spacecraft on March 5, 1980 during the period 0314-1318 UT. The data shown is typical of the majority of the events in which spectral broadening of transmitter signals was observed on satellites in the period October 1980-January 1981.

Figure 3a consists of two spectrograms that show the VLF wave data in the 0-to-10 and 9.5-to-14.5-kHz range during the period 0314:25-0315:16 UT, as the satellite moved north at mid-geomagnetic latitudes.

Wave data in the upper spectrogram consists principally of pulses from the Omega transmitter, and the entire Omega North Dakota format is clearly shown. At this point in time measurements show that the bandwidth of the Omega pulses was no more than 5 Hz (measurement uncertainty). The wave data in the lower (0-10 kHz) spectrogram of panel (a) consists principally of signals near 5 kHz from the Siple Station VLF transmitter in the Antarctic, as well as 0^+, 1^-, and 2^- whistler components [Edgar, 1976a]. Also present is a very weak lower hybrid resonance (LHR) noise band near 6 kHz which is, in general, excited by the 1^- whistler components. An example of this excitation occurs near the position of the arrow (~33-s mark) along the time axis of the 0-to-10 kHz spectrogram. It can be seen that a 1^- whistler that arrives approximately 500 ms before the arrow triggers a noist burst with a very sharp and constant lower cutoff frequency near 6 kHz. This type of excitation of the LHR noise band is a well-known feature of whistler-mode propagation [Barrington et al., 1965; Laaspere and Taylor, 1970] and is commonly used to determine the local LHR frequency in satellite data.

At the time the data of Figure 3 was acquired, the most direct propagation path to the satellite for the Omega signals consisted of an approximate 2000-km segment in the earth-ionosphere waveguide plus an approximate 1400-km segment through the ionosphere and lower magnetosphere. Using commonly accepted models of the ionosphere and lower magnetosphere [Angerami and Thomas, 1964; Strangeways and Rycroft, 1980], the calculated group time delay of signals at 13.1 and 13.6 kHz along the most direct path is approximately 100 ms.

Since the transmission time of each Omega pulse is known to better than 1 ms, the actual group time delay (T) can be measured directly from Figure 3. This measurement yields a value $T = 100 \pm 20$ ms, in good agreement with the cal-

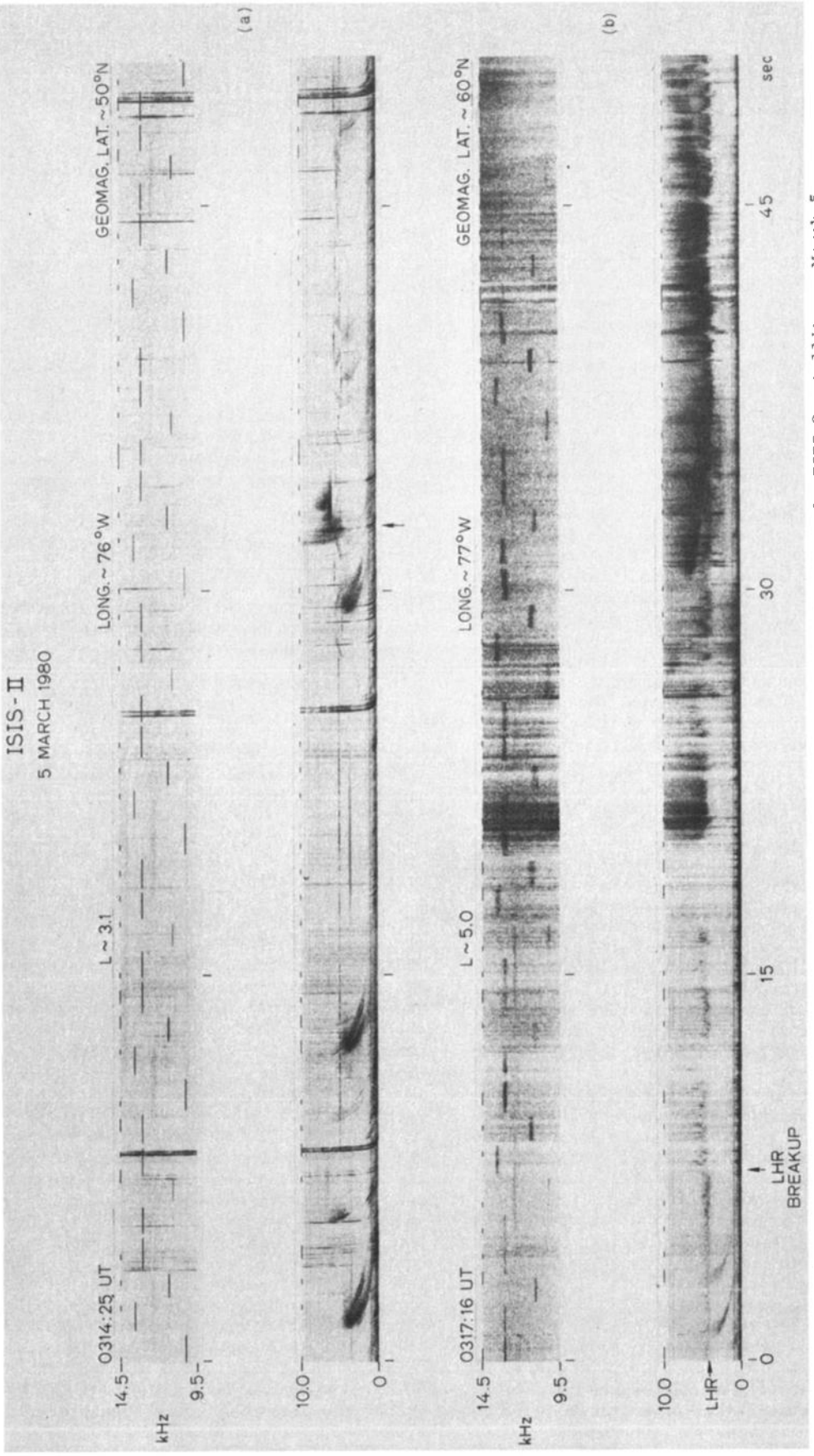

Fig. 3. Spectrograms of VLF electric field wave data acquired on the ISIS 2 satellite on March 5, 1980, showing spectral broadening of VLF transmitter signals. A timing signal appears at the top of the spectrogram.

culated value of T. Thus there is good reason to believe that the observed Omega signals propagated along a direct path through the ionosphere and lower magnetosphere to the satellite, as shown in Figure 1.

During the period 0315-0317 UT the LHR noise band slowly dropped in frequency and increased in strength, until at 0317:16 UT, as shown in the lower spectrogram of Figure 3b, the lower cutoff frequency of the LHR noise band was located near 4 kHz (see arrow on frequency axis). For the next 7 s, the lower cutoff frequency of the LHR noise band remained constant near 4 kHz, but abruptly at the 7-s mark the lower cutoff frequency jumped to 6 kHz and then became quite irregular. At the same time, impulsive bursts of VLF hiss appeared across the spectrum, extending from 0 kHz to at least 14.5 kHz. Near the 20-s mark, the irregular LHR noise band and impulsive hiss merged into a well-known VLF hiss form sometimes called a 'V shaped' hiss form [Gurnett and Frank, 1976]. This type of hiss has been shown to be associated with intense fluxes of precipitating low-energy (<1 keV) electrons [Gurnett and Frank, 1976], a fact that will be discussed below in section 3.1.

It is clear from the upper spectrogram of Figure 3b that the bandwidth of the Omega pulses exhibits a sudden increase at the same time that the LHR noise band becomes irregular. Furthermore, it is clear that all of the Omega pulses exhibit a much larger bandwidth in the presence of the irregular LHR noise band and impulsive hiss than they exhibited in the period when the LHR noise band was regular and impulsive hiss was absent. Measurements show that the bandwidth of the Omega pulses after the LHR breakup ranged from 200-400 Hz, more than two orders of magnitude higher than the nominal bandwidth of 1 Hz of these pulses. This example illustrates the impulsive VLF hiss and irregular LHR noise band that typically accompany significant spectral broadening of transmitter signals.

Figure 4 shows spectrograms of VLF wave data acquired on the ISIS 2 satellite on November 5, 1980, near 0921 UT. The top panel shows a spectrogram of wave data in the 12-to-14-kHz range. Clearly in evidence in this panel are CW signals at 13.1 and 13.6 kHz from the Omega North Dakota transmitter. The group time delay of the Omega pulses from transmitter to satellite at this time was approximately 100 ms, indicating that these signals had propagated to the satellite over a direct path through the ionosphere and lower magnetosphere.

It is clear from the upper spectrogram that during the time interval 0-18 s, the bandwidth of the Omega signals is much larger than it is in the 18-to-46-s interval. In fact, measurements indicate that the bandwidth of the Omega signals in the 18-to-46-s interval is no more than 5 Hz (5-Hz measurement accuracy), while in the remaining intervals the bandwidth lies in the 200-to-600-Hz range. Thus it is apparent that many of the Omega pulses have experienced a very significant amount of spectral broadening along their short propagation path to the satellite.

The lower panel shows a spectrogram of wave data in the 2-to-7-kHz range. The most prominent feature of the wave data in this range is

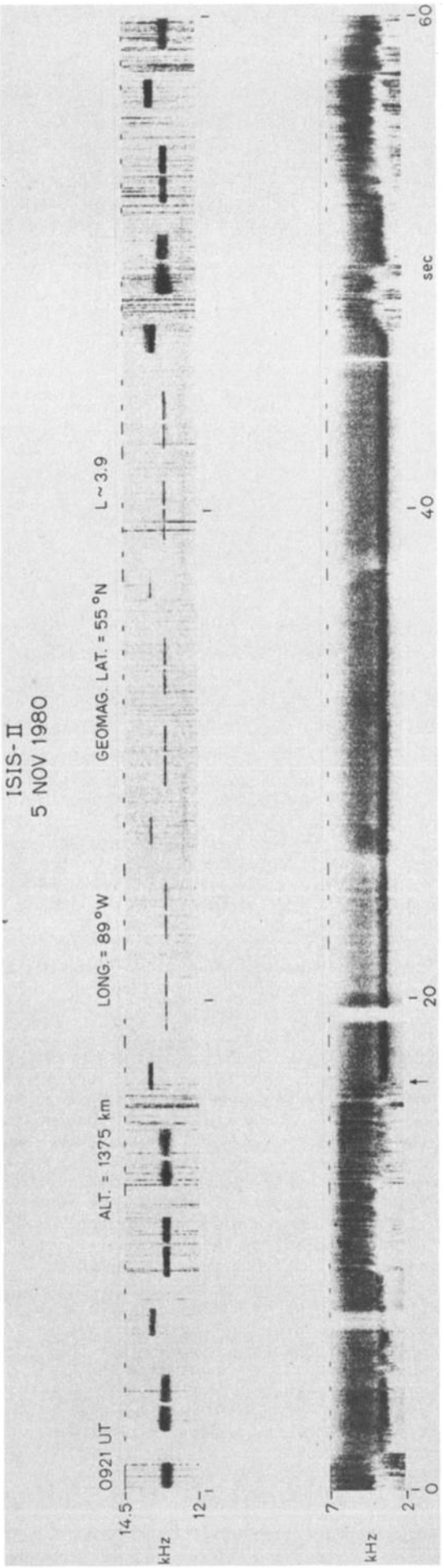

Fig. 4. Spectrograms of VLF electric field wave data acquired on the ISIS 2 satellite on November 5, 1980, showing broadening of VLF transmitter signals.

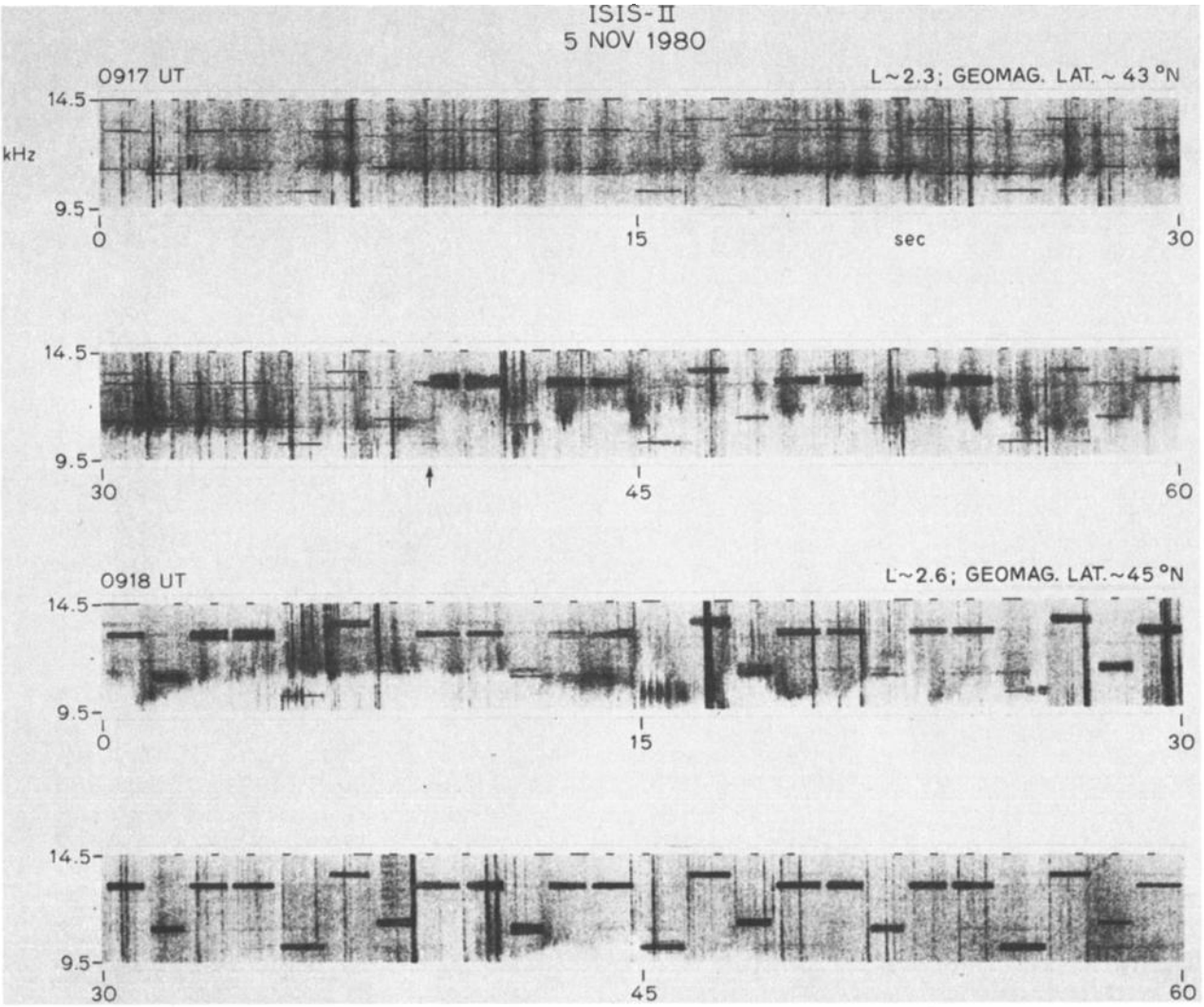

Fig. 5. Spectrograms of VLF electric field wave data acquired on the ISIS 2 satellite on November 5, 1980, showing frequency dependence of spectral broadening effect.

an LHR noise band whose lower cutoff frequency ($f_{\ell c}$) lies between 3 and 5 kHz. During the 17-to-47-s interval, $f_{\ell c}$ is sharp and constant near 3 kHz, and the noise above this cutoff consists principally of unstructured hiss. However, during the 0-to-17 and 47-to-60-s intervals, $f_{\ell c}$ fluctuates rapidly and irregularly. In addition, during these intervals, the LHR noiseband consists not of unstructured hiss but instead consists of a large number of impulsive bursts of wide-band noise of approximately 10-to-100-ms duration.

Comparison of the upper and lower panels show that, as a rule, the Omega pulses exhibit significant spectral broadening only when the LHR noise band is irregular in appearance and impulsive VLF hiss is present. When the LHR noise band is regular and impulsive VLF hiss is absent, the spectral width of the pulses is close to their nominal value at transmission. Exceptions to this rule occur only during transitions from a period of irregular noise to a period of regular LHR noise, and vice versa. For instance, an arrow on the time axis near the 17-s mark indicates the time at which a sudden transition occurs from a spectrum containing irregular LHR noise and impulsive hiss to a spectrum of regular LHR noise. It can be seen from the top panel that an Omega pulse at 13.6 kHz exhibits significant spectral broadening during a 1-s period following this transition time. Furthermore, it can be seen that a pulse at 13.6 kHz exhibits significant spectral broadening approximately 1 s before a sudden transition at the 47-s mark from regular LHR noise to irregular LHR noise and impulsive VLF hiss.

2.2. Frequency Dependence

Some important features of the frequency dependence of the spectral broadening effect are illustrated in Figure 5, which shows spectrograms of VLF wave data acquired on ISIS 2 on November 5, 1980, approximately 4 min before the data shown in Figure 4. Each of the four panels in the figure involves a 30-s interval of wave data in the 9.5-to-14.5-kHz range and together they show a continuous 2-min portion of wave data.

Wave data in the upper panel consists principally of CW signals from the Omega North Dakota transmitter, a regular LHR noise band with moderately well-defined lower cutoff frequency ($f_{\ell c}$) and occasional 0^+ whistler traces. The LHR noise band is not strong, but $f_{\ell c}$ is easily discerned as lying close to 11 kHz. The Omega pulses are for the most part somewhat difficult to discern since they generally lie within the LHR noise band. However, the pulses at 10.2 kHz lie below the noise band and three of these can be seen arriving at the 5-, 15-, and 25-s marks. None of the Omega pulses at this time exhibit significant spectral broadening.

In the second panel, an arrow on the time axis marks the time, 39 s, at which a sudden transition occurs between the period of regular LHR noise and a second period of irregular LHR noise and impulsive VLF hiss. At the position of the arrow within 200 ms), $f_{\ell c}$ jumps from 11 to 12.5 kHz, and almost simultaneously the bandwidth of the Omega pulse at 13.1 kHz increases to 500 Hz. After this transition point all Omega pulses that lie above $f_{\ell c}$ exhibit significant spectral broadening, while those that lie below this cutoff exhibit little or no additional spectral broadening. This feature of the data can be appreciated by visually comparing the bandwidth of the Omega pulses at 10.2 kHz (arriving at the 45- and 55-s marks), which lie below $f_{\ell c}$, with that of the pulses at 13.1 and 13.6 kHz that lie within the noise band.

In the second panel it can be seen that none of the pulses at 11.05 kHz (which arrive at the 31-, 41-, and 51-s positions) exhibit significant broadening since these pulses lie below the LHR noise band. However, in the third panel the noise band drops momentarily below 11.05 kHz just before the 1-s mark and the spectrum of the arriving pulse at 11.05 kHz is quite broad. In the third panel, after 0918:20 UT, $f_{\ell c}$ begins to decrease on the average and by 0918:26 UT has dropped below 9.5 kHz. From this point in time all pulses lie within the irregular noise band and all exhibit significant spectral broadening. This feature is shown clearly in the fourth panel (the format of panel four can be used to identify the locations of any Omega pulses in the upper panels that are obscured because of the presence of the LHR noise band).

It is commonly believed that the lower cutoff frequency of the LHR noise band is equal to the local value of the LHR frequency at the satellite location [Smith and Brice, 1964]. If this is true, then data such as that shown in Figure 5 demonstrates that the spectral broadening effect occurs only for those transmitter signals whose frequency exceeds the local LHR frequency at the satellite location.

It is noteworthy that when spectral broadening is observed to occur, it occurs for signals distributed over a wide range of frequencies. For instance, Figure 6 shows a typical case in which spectral broadening is observed simultaneously in signals from the Omega, North Dakota, NAA, and NLK (18.6 kHz) transmitters, covering approximately an 8-kHz range in frequency. At the time shown, the spacecraft was located at a geographic longitude of 85°W; thus the signals from station NLK (Jim Creek, Washington; 48°N, 122°W) traversed a path in the earth-ionosphere waveguide of ~3000 km before reaching the subsatellite point.

2.3. Antenna Orientation Dependence

The bandwidth of the spectrally broadened signals often shows a strong dependence on the orientation angle of the dipole antenna with respect to the local direction of the earth's magnetic field. Figure 7 displays an example of the effect as seen in ISIS 2 data from August 14, 1979, near 0813 UT. The upper panel of the figure shows a spectrogram of the VLF wave spectrum in the 0-to-20-kHz range over a 30-s time period. The spectrum consists principally of signals from the Omega, North Dakota, transmitter, and station NAA (17.8 kHz), as well as an irregular noise band with lower cutoff frequency near 8 kHz, a narrow band of chorus near 6 kHz, and a narrow band of chorus near 1 kHz. Figure 7b shows a simultaneous spectrogram of increased frequency resolution which covers the range 9.5-to-14.5 kHz. In this range, the Omega signals are dominant features of the spectrum, and the large bandwidth of these signals is clearly in evidence.

Figure 7c shows a simultaneous spectrogram covering the 12.5-to-13.7-kHz range. In this range the Omega signals at 13.1 kHz can be seen very clearly, and the lower half of the Omega signals at 13.6 kHz are also visible. It is evident that the bandwidth of the signals at 13.1 varies markedly with time, reaching a maximum twice each spin period (period ~19 s) near the times at which the receiver output signal approaches the noise level (spin null). This signal drop-out occurs when the satellite dipole antenna is aligned approximately parallel to the local direction of the earth's magnetic field, as shown in Figure 8.

Figure 8a shows the bandwidth (10 dB) of the envelope of the Omega signals at 13.1 kHz, as measured from spectrum analyzer A-scan records. Figure 8b depicts the angle ϕ between the dipole antenna and the local direction of the earth's magnetic field $\overline{B}_o$ as derived from onboard magnetometer data. The accuracy of the angular plot is approximately ±5°.

Comparison of Figures 8a and 8b shows that the maximum bandwidth of the Omega signals occurs near the times when $\phi \sim 0°$ or 180°, i.e., near the time when the antenna is parallel to $\overline{B}_o$. It is also clear that the minimum bandwidth of the signals occurs when $\phi \sim 90°$ and the antenna is perpendicular to $\overline{B}_o$.

Although the signal bandwidth reaches a maximum near the points $\phi \sim 0°$ and 180°, it tends to approach zero whenever the antenna is closely parallel to $\overline{B}_o$ and the signal amplitude is low (spin nulls). This effect can be seen in Figure 7b, where two Omega pulses at 11.3 kHz fall within the spin null periods near the 12- and 22-s marks. Both pulses show amplitude fading accompanied by irregular bandwidth decreases. As a general rule it was found during our study that all transmitter pulses, both normal and spectrally broadened, showed much smaller electric field amplitudes in the spin null positions where the satellite antennas were closely parallel to $\overline{B}_o$. This finding indicates that the wave electric field parallel to $\overline{B}_o$ is always much smaller than that perpendicular to $\overline{B}_o$, a result in keeping with the

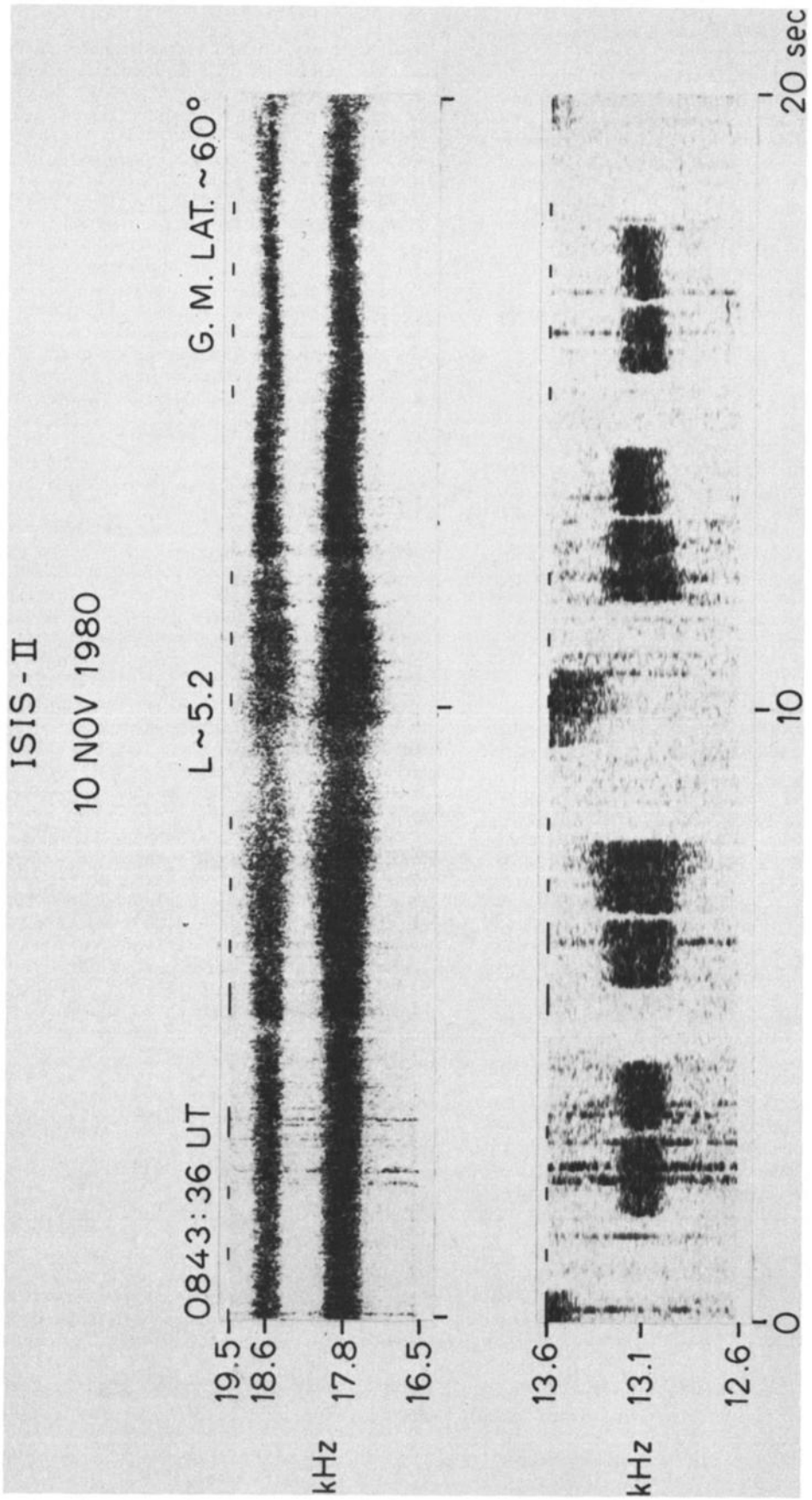

Fig. 6. Spectrograms of VLF electric field wave data acquired on the ISIS 2 satellite on November 10, 1980, showing simultaneous spectral broadening of signals from three transmitters.

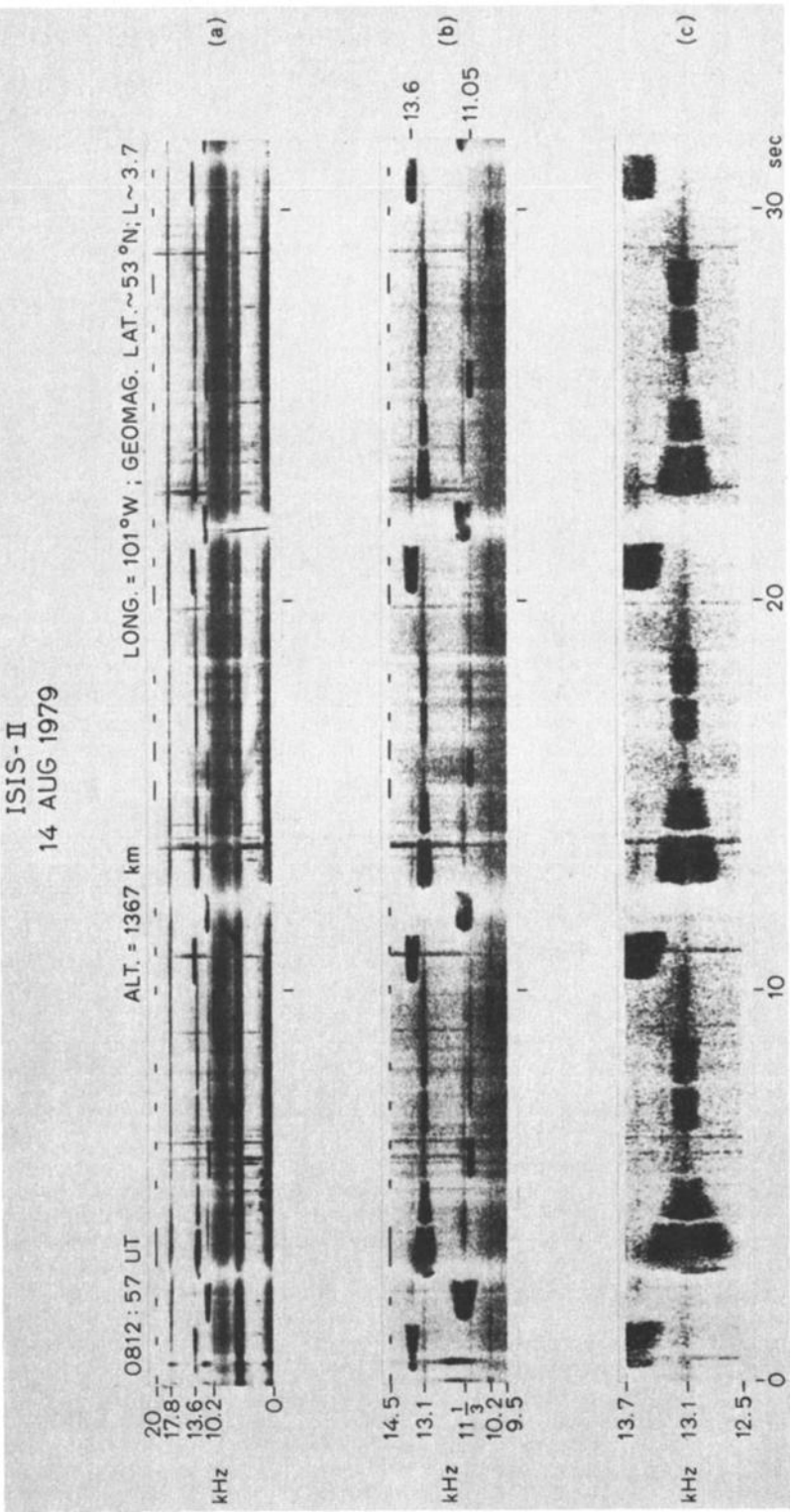

Fig. 7. Spectrograms of VLF electric field wave data showing dependence of signal bandwidth on dipole antenna orientation.

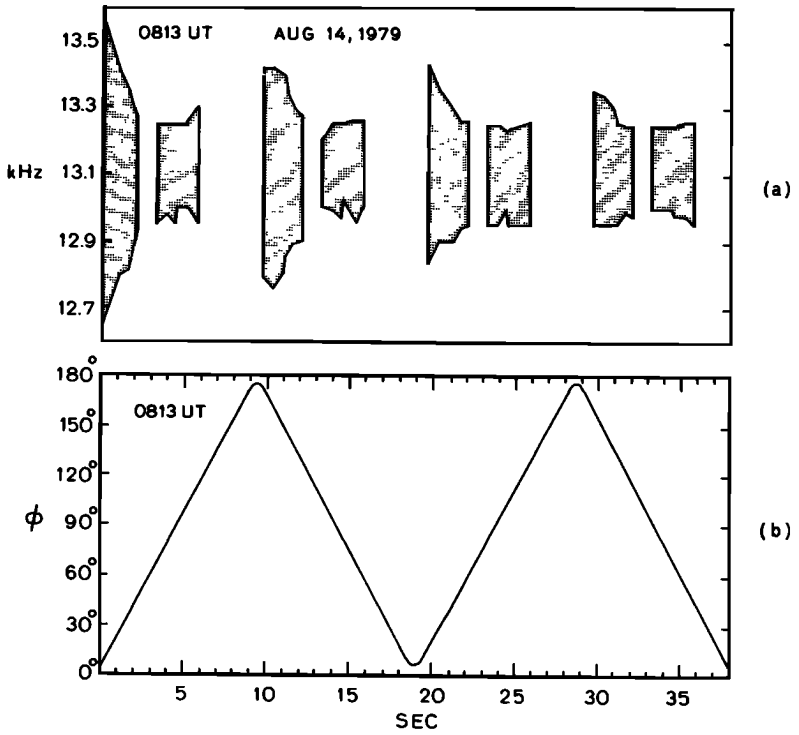

Fig. 8. Plots made from ISIS 2 data acquired on August 14, 1979. (a) The spectral bandwidth of 16 Omega transmitter pulses (hatched regions) at a nominal frequency of 13.1 kHz. (b) A plot of the angle ϕ between the electric dipole antenna axis and the local direction of the earth's magnetic field $\vec{B}_o$. Bandwidth maxima occur when antenna is nearly parallel to $\vec{B}_o$.

theory of whistler-mode propagation in a cold plasma [Stix, 1962; Helliwell, 1965].

In addition to the strong upgoing direct Omega pulses shown in Figure 7, there are also weak two-hop (2^- mode) downgoing echoes of these pulses present in the data. The echoes can be seen fairly clearly in Figure 7b, occurring approximately 2 s after each pulse at 11.05, 11.3, and 13.6 kHz.

The direct signals and the echoes can be readily differentiated in at least two ways. First of all, the group time delay of the direct upgoing pulses (100 ms) is much shorter than the group time delay of the echoes (2 s). Second, the duration of the direct pulses is generally within 100 ms of their nominal duration while the echoes are highly dispersed in time with duration of up to 2-3 times the nominal value.

2.4. Chevron Form

It is important to note from Figures 7b and 7c that the Omega pulses have a spectral envelope that has a characteristic 'chevron' shape which is roughly symmetric about the carrier. This shape results from the fact that the time delay of each spectral component at frequency f is an increasing function of the difference frequency $\Delta f = |f - f_c|$, where f_c is the nominal carrier frequency of the pulse.

Figure 9a shows a high-resolution spectrogram of one of the 11.3 kHz Omega pulses shown in Figure 7b. This pulse is typical of those that show significant spectral broadening.

Figure 9b shows schematically the characteristic chevron shape of the envelope of the pulse shown in Figure 9a. In general, the time delay varies approximately linearly as Δf, and the envelope of the leading edge of each pulse can be described by the two variables γ and Δf_m, where γ is the slope of the leading edge of the pulse (referred to the frequency axis), and Δf_m is the difference frequency between the component at the carrier frequency f_c and the component at the lower (or upper) boundary of the envelope of the leading edge of the pulse. With these variables, the differential time delay δ between a component at f and the component at f_c can be described by the relations:

$$\delta = \tan\gamma\Delta f \qquad 0 \leq \Delta f \leq \Delta f_m$$

(where Δf is expressed in kHz and δ is expressed in seconds). A similar relationship holds for the trailing edge of each pulse.

For the particular data shown in Figure 7b, γ has the value $12° \pm 2°$, and for each pulse the maximum value of δ, δm, lies in the range 50 ms $< \delta_m <$ 150 ms.

The fact that $\delta_m \neq 0$ suggests that the off-carrier spectral components of each pulse may have been generated at altitudes significantly below the spacecraft and subsequently experienced dispersion while propagating to the satellite.

However, this dispersion is not what one would normally expect for whistler-mode waves of differing frequency. For instance, if the dispersion is due to a true frequency difference between the pulse components and these components are generated at approximately the same altitude, we would expect the dispersion to follow the usual whistler-

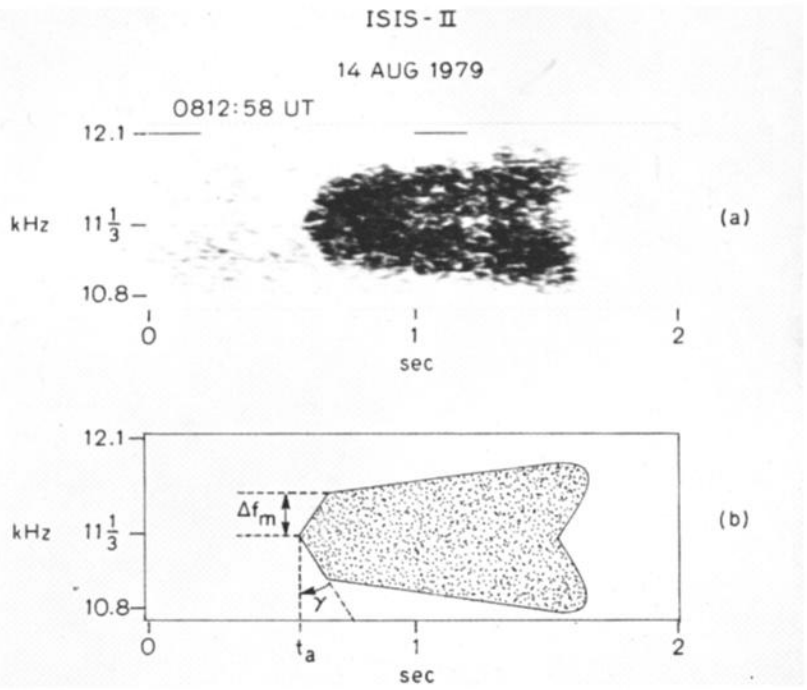

Fig. 9. (a) High-frequency resolution spectrogram showing 'chevron' shape of the pulse envelope of spectrally broadened signals. (b) Schematic representation of pulse in (a). The magnitude of the angle γ gives a measure of the dispersion of the sideband components of the pulse.

mode relation [Helliwell, 1965] $\tau \sim f^{-\frac{1}{2}}$, where τ is the whistler-mode time delay and f is the wave frequency. However, the measured dispersion is roughly symmetric about the carrier frequency of each pulse for carrier frequencies that range between 10.2 and 13.6 kHz, and does not conform to the $f^{-\frac{1}{2}}$ law.

Furthermore, the dispersion between the carrier and the sidebands is extremely large for the short propagation paths characteristic of the observations. For instance, in the example shown in Figure 9, the maximum dispersion between the sideband and carrier components is approximately equal to the propagation time of the carrier between the transmitter and the satellite.

In view of these considerations, it is not likely that the dispersion in the pulses arises from frequency differences between the pulse components. Instead, as discussed in section 3.3, we interpret the dispersion to be due to differences in group velocity between waves of equal frequency but differing wave vectors $\bar{k}$ which have been scattered by irregularities near the F layer.

2.5. Pulse Power Spectrum

Measurements of the power spectral density of the spectrally broadened Omega pulses showed three basic characteristics:

1. At any given time the electric field intensity of a spectrally broadened signal tended to peak at a discrete set of frequencies on both sides of the nominal carrier frequency. However, the position and amplitude of the sidebands varied with time.

2. In many cases, the electric field amplitude reached a minimum near the nominal carrier frequency of the pulses.

3. Often, the amplitude distribution was roughly symmetric about the nominal frequency; however, many clear cases of asymmetry were also observed.

These characteristics are observed in Figures 10 and 11. Figure 10 shows a series of amplitude measurements of two spectrally broadened pulses, each of which has a nominal carrier frequency of 13.1 kHz. The amplitude is shown across an 800-Hz frequency range centered on the carrier. Each spectral scan is carried out in 8 ms, and scans are repeated every 50 ms. Approximately 1 s of data are shown for each pulse. The amplitude on each scan is measured on a logarithmic scale with respect to the sloping base line. The position of the carrier frequency is indicated by an arrow perpendicular to the frequency axis. It can be seen in both cases that the wave energy tends to peak at a discrete set of frequencies and that these sidebands are distributed roughly symmetrically about the carrier frequency. It is evident that the sideband locations change slowly with time.

Figure 10a shows a typical case of spectral broadening in which the amplitude at the nominal carrier frequency (13.1 kHz) is generally at least as high as the amplitude of the strongest sideband components. Figure 10b shows a typical case in which an amplitude minimum occurs near, or at, the nominal carrier frequency.

In order to investigate the long-term relationship between the sideband components and the carrier, it is useful to consider the average power spectral distribution in each pulse.

Figure 11 represents six plots ((a)-(f)) of some common average power spectral distributions observed in Omega transmitter pulses exhibiting spectral broadening. The power spectral dis-

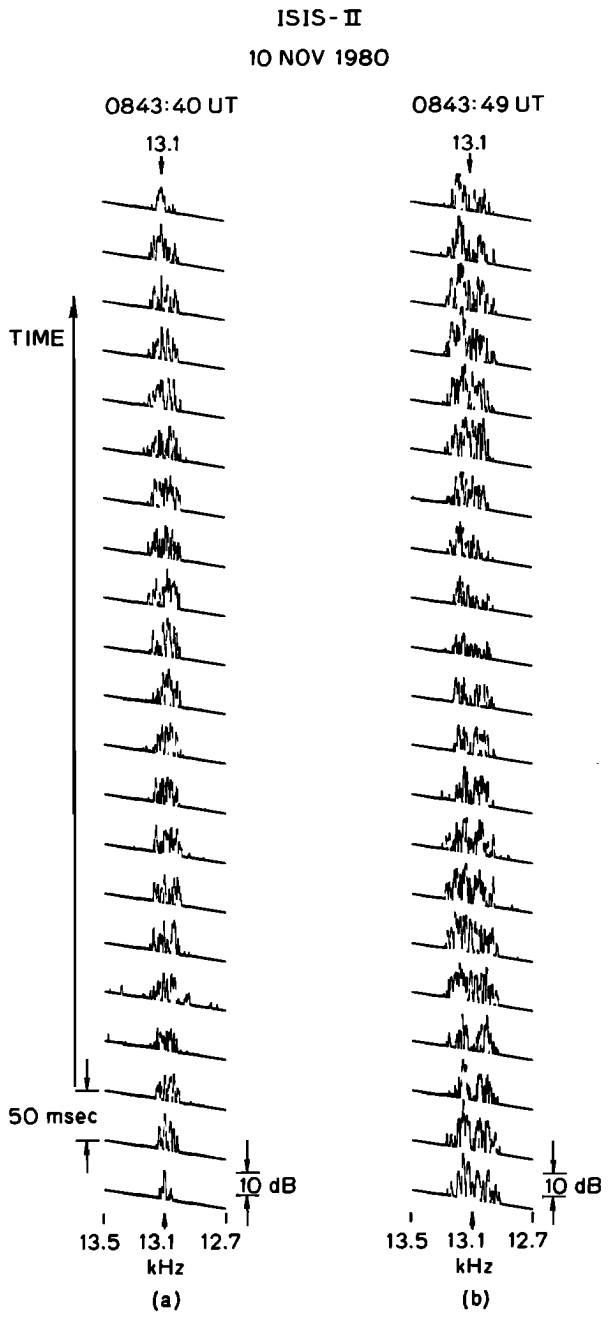

Fig. 10. A-scan records showing wave electric field amplitude as a function of frequency every 50 ms for two transmitter pulses of nominal frequency, 13.1 kHz. In (a) the amplitude at the carrier frequency is generally higher than that of the sidebands. In (b) the amplitude at the carrier frequency is generally much lower than that of the sidebands.

tribution (signal level) is plotted as a function of the difference frequency $\Delta f_D = f - f_c$, where f_c is the nominal carrier frequency (Note: in the case of Figure 11f the abscissa represents frequency).

To prepare these plots, a digital spectrum analyzer was used to determine the power spectral distribution in five consecutive 200-ms samples of each pulse. These distributions were then averaged to obtain the average power spectral distribution. Use of the digital analyer allowed a frequency resolution of approximately 6 Hz.

Figure 11a shows a common case in which the carrier is suppressed more than 10 dB below the two broad, relatively unstructured, sidebands located approximately ~100 Hz from f_c. Figure 11b shows the case of a deep minimum near f_c and sidebands with relatively more structure. Figure 11c shows a common case of suppressed carrier and markedly asymmetric sidebands. Sideband suppression can occur for both positive and negative Δf_D. Figure 11e shows a common case of partially suppressed carrier in which the amplitude minimum occurs at a frequency slightly removed from the nominal carrier (in the case shown, the minimum occurs approximately 20 Hz above the carrier frequency). Figure 11d shows the average power spectral distribution of two 52-s portions of the signal from the NAA transmitter. The earlier sample (0836:53 UT) was taken at a time when no spectral broadening was observed in either Omega or NAA signals. The later sample (0843:33 UT) was taken when significant broadening was observed in both the Omega and NAA signals. It can be seen that the normal NAA signal has a 10-dB bandwidth of ~200 Hz, while the time averaged spectrally broadened signals was a 10-dB bandwidth of 400 Hz. However, since the signal bandwidth of the spectrally broadened signal varies with time, a temporal average will underestimate the amplitude of the sideband components which are farthest from the carrier. Thus the maximum bandwidth during any one spin period will exceed that shown on the plot (e.g., see bandwidth variation in Figure 6).

It is interesting that the NAA signal does not show a minimum near the carrier frequency, as do the Omega pulses. This difference is attributed to the fact that the frequency range over which carrier suppression takes place, ~50 Hz, is less than the sideband separation in the normal NAA signal.

2.6. Relation to Impulsive ELF Hiss

Spectral broadening was often observed in association with a band of weak ELF impulsive hiss below 700 Hz whose upper cutoff frequency depended strongly upon the orientation of the dipole antenna with respect to the local direction of the earth's magnetic field. Examples of this association are shown in Figures 12 and 13.

Figure 12a shows a spectrogram whose dominant feature is a band of impulsive hiss with an upper cutoff frequency that varies between 200 and 500 Hz. The bandwidth maximum occurs twice every spin period at the position in which the antenna is closely parallel to $\overline{B}_o$, and the bandwidth minimum occurs when the antenna is perpendicular to $\overline{B}_o$. This type of ELF impulsive hiss was observed quite often at high latitudes beyond the plasmapause and was generally associated with irregular LHR noise bands and impulsive VLF hiss at higher frequencies. In general, it was one of the dominant features of the wave spectrum at high latitudes. This hiss band was often also present at lower latitudes, at a much lower amplitude level, and often appeared in association with the spectral broadening of the transmitter pulses.

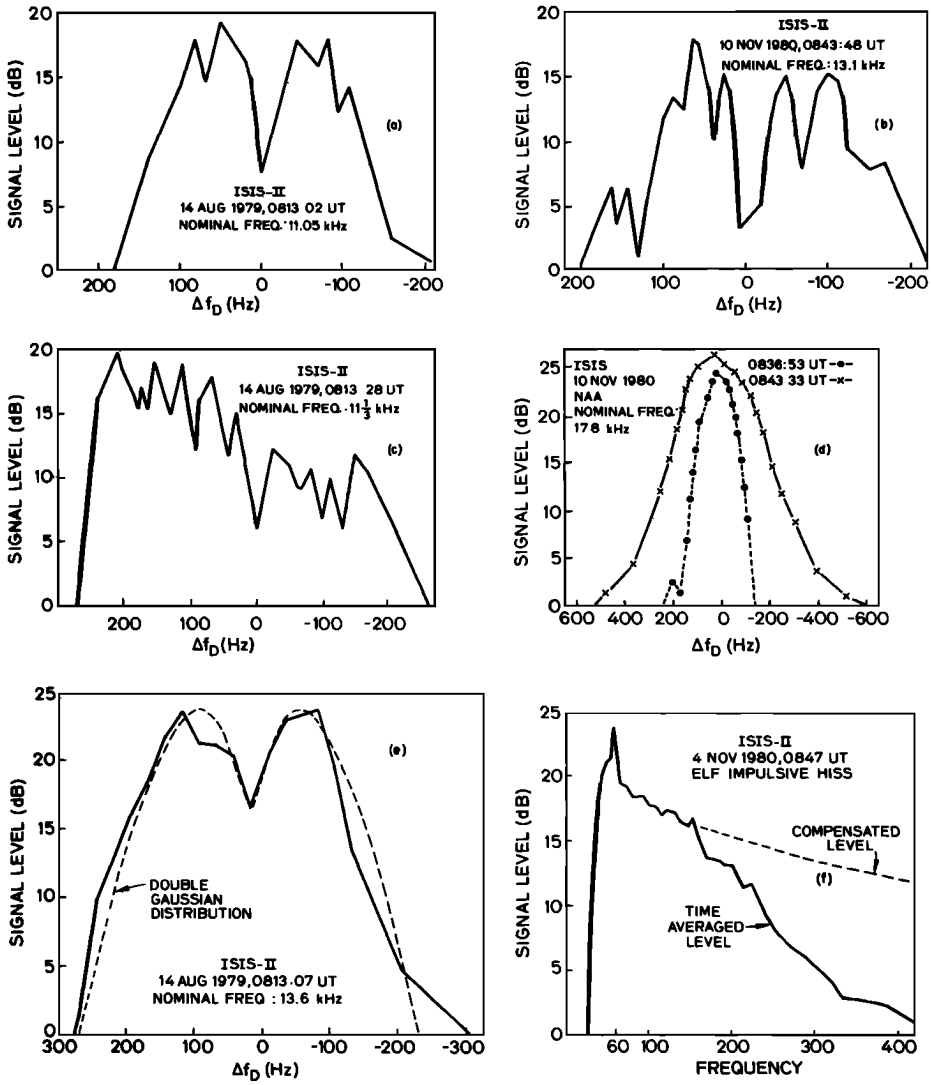

Fig. 11. Average power spectral density for five common cases of spectrally broadened transmitter signals and one example of impulsive ELF hiss. (a) Spectrally broadened Omega North Dakota pulse with partially suppressed carrier and roughly symmetric, relatively unstructured sidebands. (b) Spectrally broadened Omega North Dakota pulse with more fully suppressed carrier and more highly structured sidebands. (c) Spectrally broadened Omega North Dakota pulse with partially suppressed carrier and asymmetric sidebands. (d) Average power spectral distribution of two 52-s samples of signals from the NAA transmitter. The earlier sample (0836:53 UT) was taken at a time when no spectral broadening was observed in either Omega or NAA signals. The later sample was taken when significant broadening was observed in both the Omega and NAA signals. (e) Spectrally broadened Omega North Dakota pulse with partially suppressed carrier and roughly symmetric sidebands. Amplitude minimum occurs approximately 20 Hz above carrier frequency. Curve in dashed line corresponds to fitted double Gaussian distribution discussed in the appendix. (f) Example of power spectrum of impulsive ELF hiss. Peak at 60 Hz is due to local interference line introduced in the ground recording. Compensated curve corrects for signal bandwidth change due to dipole antenna rotation.

Figure 12b shows two simultaneous spectrograms of the wave data in the ranges 13.1-to-13.7 kHz and 0-to-600 Hz for a 40-s period near 1813 UT. The data shown in the upper spectrogram of Figure 12b represents the wave energy in the upper half envelope of the Omega pulses at 13.1 kHz depicted in Figure 7c. Only the upper half envelope is shown in order to display more clearly the correlation between the bandwidth of the Omega signals and the bandwidth of the impulsive hiss.

Comparison of the upper and lower spectrograms of Figure 12b shows that the bandwidth of the weak impulsive hiss varies in the same manner as that of the Omega pulses as the antenna rotates in the earth's magnetic field. Furthermore, at

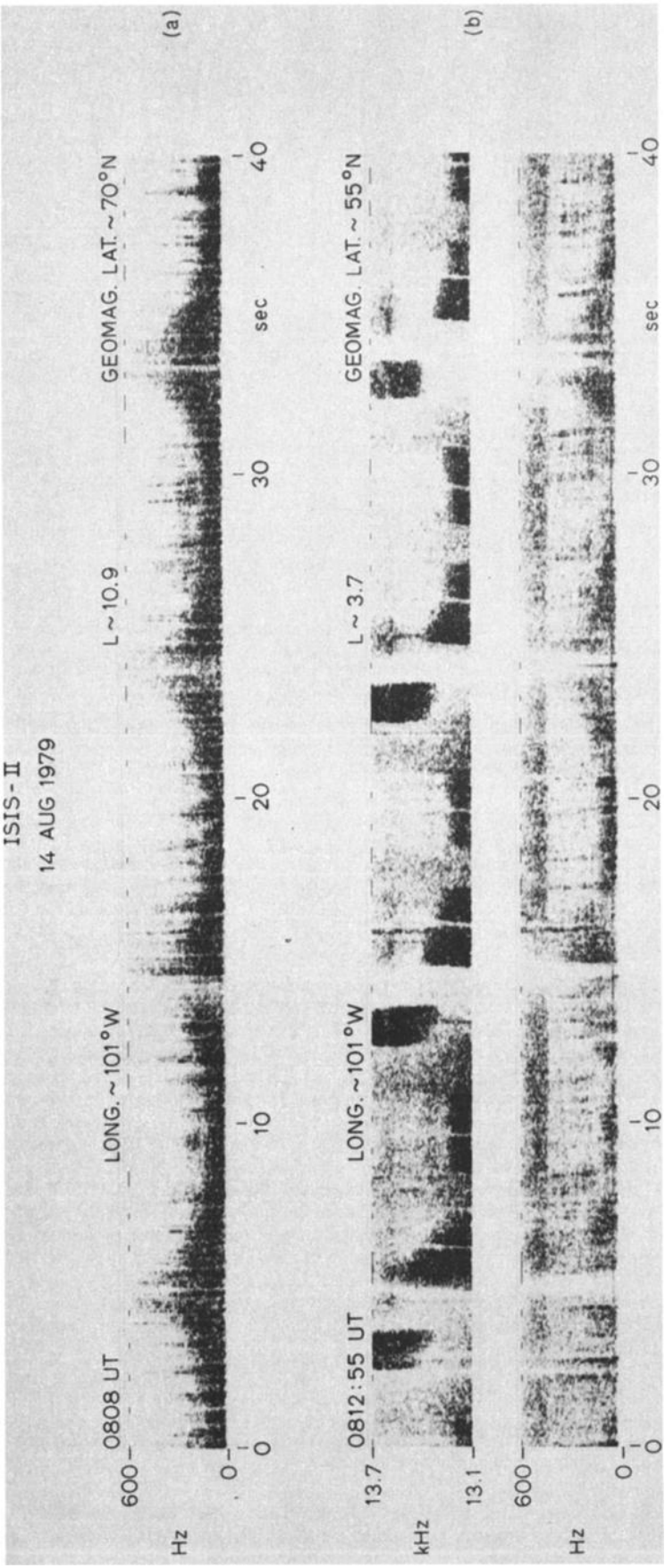

Fig. 12. Spectrograms of VLF electric field wave data acquired on ISIS 2 on August 14, 1979. (a) Band of impulsive VLF hiss with periodic variation of its upper cutoff frequency at half the satellite spin period, as detected at high-geomagnetic latitude. (b) Mid-latitude observation of simultaneous electric field data at VLF and ELF. The upper spectrogram shows the upper half envelope of the Omega transmitter pulses of nominal frequency 13.1 kHz. The lower spectrogram shows a band of impulsive ELF hiss below 600 Hz. The upper cutoff frequencies of the hiss band and the pulse envelope vary in a similar manner.

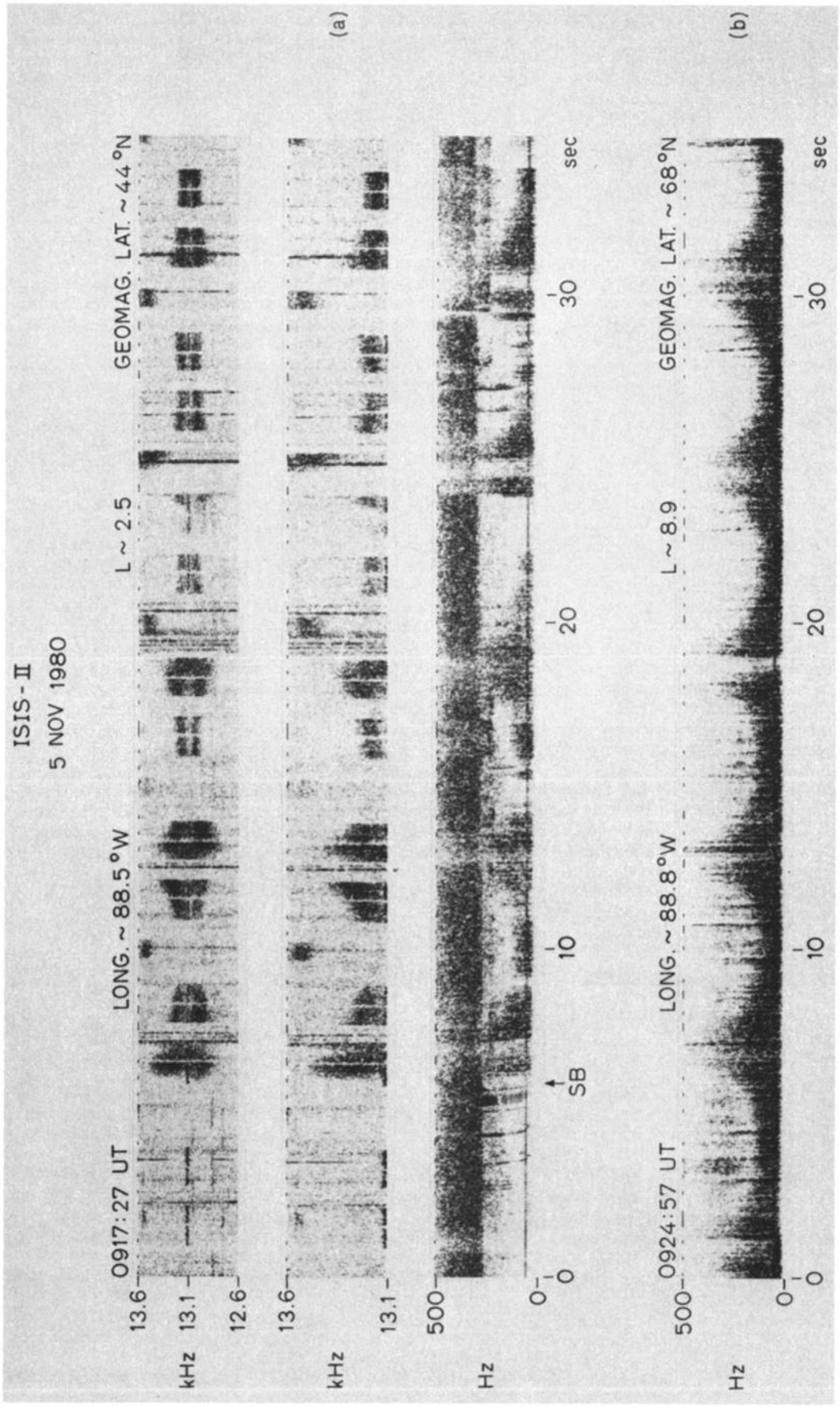

Fig. 13. Spectrograms of VLF electric field wave data acquired on ISIS 2 on November 5, 1980. (a) Simultaneous electric field data in three frequency bands. The upper spectrogram shows the spectral broadening associated with Omega transmitter pulses at 13.1 kHz. The middle spectrogram shows the upper half-envelope of the same Omega pulses. The lower spectrogram shows a band of impulsive ELF hiss below 300 Hz. The upper cutoff frequencies of the hiss band and the upper half of the pulse envelope vary in a similar manner. (b) Impulsive ELF hiss band at a later time outside the plasmapause.

most times the bandwidth measure of the weak impulsive hiss is within 60% of the half-bandwidth of the Omega signals.

A second example of the association of the ELF impulsive hiss with the spectral broadening phenomenon is given in Figure 13, which shows four spectrograms of wave data acquired on the ISIS 2 spacecraft on November 5, 1980.

The upper spectrogram of Figure 13a depicts Omega transmitter signals at 13.1 kHz over a 35-s time period near 0917:27 UT. (The same data are shown in a compressed format in the second spectrogram of Figure 5). The middle spectrogram of Figure 13a depicts the wave energy in the upper half envelope of the Omega pulses at 13.1 kHz shown in the upper spectrogram. The lower spectrogram of Figure 13a shows the simultaneous ELF wave spectrum below 500 Hz.

It is clear from Figure 13a that Omega pulses at 13.1 kHz that occur during the first 6 s show no sign of significant spectral broadening. However, a sudden bandwidth increase occurs at the point marked by the arrow (SB) on the time axis. This sudden increase was discussed above in connection with Figure 5 and the sudden onset of LHR noise band irregularities. From Figure 13a it can be seen that the sudden bandwidth increase is also accompanied by the abrupt appearance of weak ELF impulsive hiss whose bandwidth is roughly equal to one-half of that of the Omega pulses and is spin-modulated in a manner identical to that of the Omega pulses.

Figure 13b shows a spectrogram of wave data acquired at a slightly later time when the satellite had reached a geomagnetic latitude of 68°N. At this point the impulsive ELF hiss had become one of the dominant features of the wave spectrum in a region where the Omega pulses were no longer detected.

A typical example of the average (2 min) power spectral density of the impulsive ELF hiss beyond $L \sim 4$ is shown in Figure 11f. When compensated for temporal bandwidth variations, the power distribution falls off smoothly and slowly with frequency. The peak at 60 Hz is due to local interference at the recording site. The drop-off below 50 Hz is due to receiver characteristics.

2.7. Additional Observations and Occurrence Patterns

Although most examples of the spectral broadening effect have been obtained from ISIS 2, good examples have also been obtained from the ISIS 1 and ISEE 1 spacecraft.

Figure 14 shows two examples of ISIS 1 data in which the spectral broadening effect is clearly shown. Figure 14a shows a mid-latitude event consisting of the spectral broadening of Omega transmitter signals with maximum bandwidth approaching 600 Hz. The upper spectrogram of Figure 14b shows a high latitude event consisting of the spectral broadening of signals from the NAA transmitter at 17.8 kHz. At this time the subsatellite point was close to the location of the transmitter (geographic longitude ~68°W, geomagnetic latitude ~57°N) and the transmitter signal was the dominant feature of the 9.5-to-19.5 frequency range. The lower portion of Figure 14b shows a higher resolution spectrogram of the data shown in the upper portion. It can be seen that the maximum bandwidth of the NAA signal approaches 2 kHz, while the minimum bandwidth is close to 300 Hz, approximately 50% larger than the nominal 200-Hz bandwidth of the NAA signal. It should be noted that the NAA signal most probably consists entirely of the direct component, since the relatively high latitutde of observation precludes conjugate echoes.

Figure 15 shows an example of spectral broadening acquired on the ISEE 1 spacecraft on August 6, 1981, at an altitude of approximately 2700 km. The upper spectrogram of Figure 15a shows the wave data in the 0-to-15-kHz range over a 30-s period. At this time signals from the Omega transmitter at North Dakota are in evidence as well as an LHR noise band with a regular cutoff frequency near 5 kHz (marked by an arrow on the frequency axis). Also present is a hiss band extending from 2 to 7 kHz. Since the satellite spin period is approximately 3 s, spin nulls in the wave data appear every 1.5 s as the dipole antenna periodically comes within 30° of $\overline{B}_0$. The lower spectrogram of Figure 15a shows the Omega pulses at 13.1 kHz in a 500-Hz band, and it is clear from this spectrogram that the bandwidth of the Omega pulses is no more than 30 Hz, a value equal to the frequency resolution of the spectrogram. The upper spectrogram of Figure 15b shows the wave data in the 0-to-15-kHz range approximately 1 min later. The LHR noise band has developed an irregular lower cutoff frequency and impulsive VLF hiss has appeared in the spectrum. At the same time, as shown in the lower spectrogram of Figure 15b, the bandwidth of the Omega pulses has increased to approximately 200 Hz and exhibits a small amount of dependence upon the antenna orientation angle.

Notice that five of the Omega pulses at 13.1 kHz (at 6.3, 12.5, 14.0, 26.4, and 27.7 s) span a spin null location, and the amplitude of the pulses at those locations drops below the background noise levels. This supplies further evidence that the electric vector of the spectrally broadened waves lies mainly perpendicular to $\overline{B}_0$.

The spatial distribution of observations of the spectral broadening effect is shown in Figure 16. Figure 16a depicts the geographic longitude and invariant geomagnetic latitude of the ISIS 1 satellite during periods of spectral broadening of VLF transmitter pulses, and Figure 16b shows the same variables for ISIS 2 events.

In these coordinates, the satellite track for each orbit is close to a straight line at constant longitude. Each line section shown in the plots represents the points along each satellite track at which spectral broadening events were observed. It can be seen from the figure that events were observed over a wide range of geographical longitudes and geomagnetic invariant latitudes. However, most observations occurred beyond the average plasmapause location [Carpenter, 1966] at invariant latitudes greater than 60°. The apparent drop-off in occurrence at roughly 90°W arises because passes farther west were not routinely covered by the Ottawa telemetry station for the period under study. The true occurrence of broadening is not thought to have this longitudinal dependence.

With few exceptions, in all the events shown spectral broadening was observed simultaneously in both NAA and North Dakota Omega signals, as

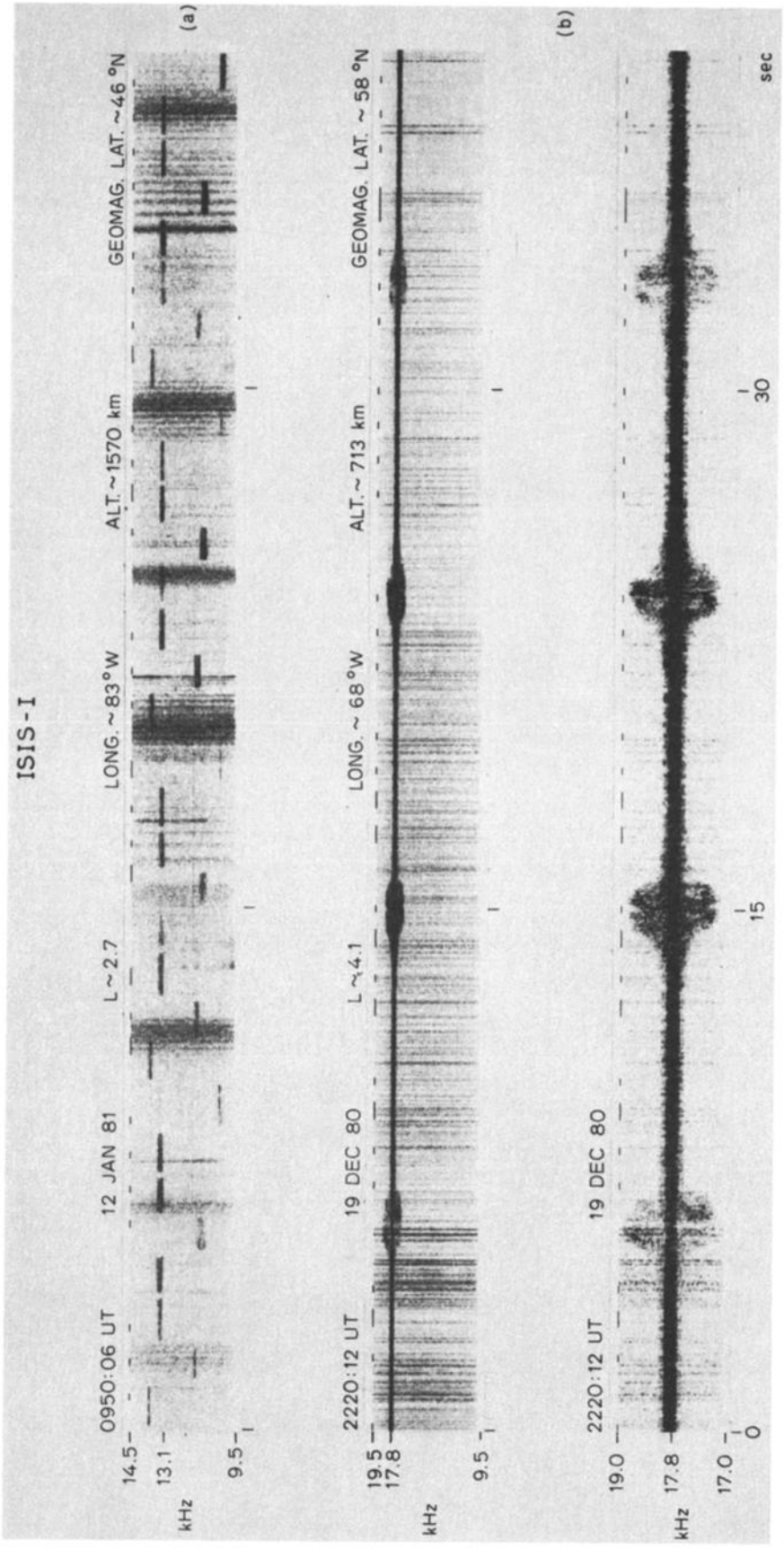

Fig. 14. Spectrograms of VLF electric field wave data acquired on ISIS 1. (a) Spectral broadening of Omega transmitter signals very similar to that seen on ISIS 2 at comparable altitudes. (b) Two spectrograms that show the spectral broadening of NAA transmitter signals at 17.8 kHz at a relatively low altitude of 713 km and at a longitude close to that of the transmitter. The upper spectrogram shows the wave activity in the 9.5-to-19.5-kHz range. Signals from the Omega North Dakota transmitter are not in evidence and the NAA signal dominates the band. Large-scale spectral broadening occurs at times when the dipole antenna is almost parallel to the direction of the earth's magnetic field (6-, 15-, 24-, and 33-s marks). The lower spectrogram shows the NAA signal with higher frequency resolution. The maximum signal bandwidth is approximately 2 kHz.

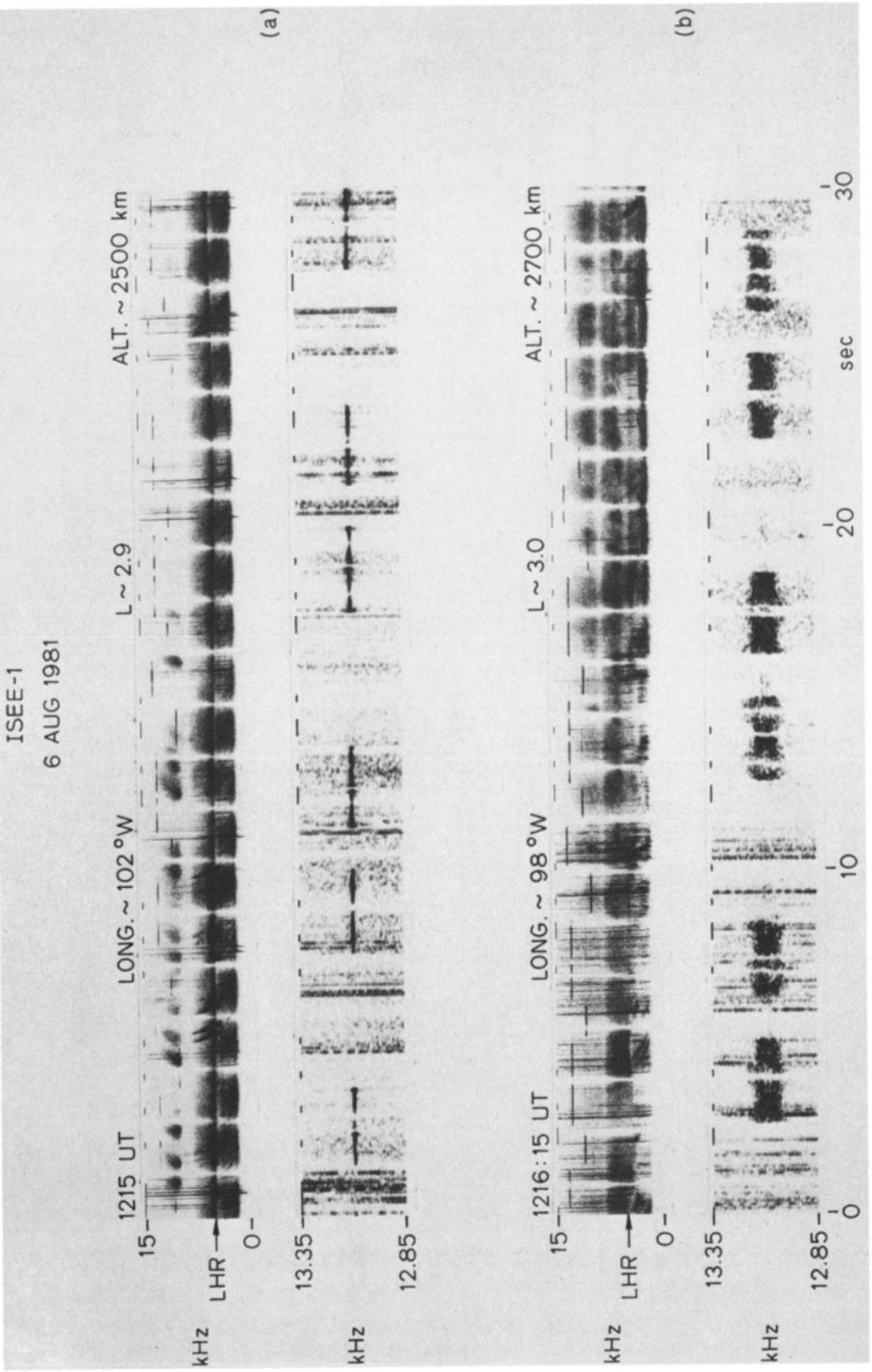

Fig. 15. Spectrograms of VLF electric field data acquired on the ISEE 1 satellite on August 6, 1981. (a) Upper spectrogram shows the wave spectrum slightly before the spectral broadening event and the lower spectrogram shows the Omega signal at 13.1 kHz with higher frequency resolution. (b) Upper spectrogram shows the wave spectrum during the spectral broadening event and the lower spectrogram shows the broadened pulses at 13.1 kHz with higher frequency resolution.

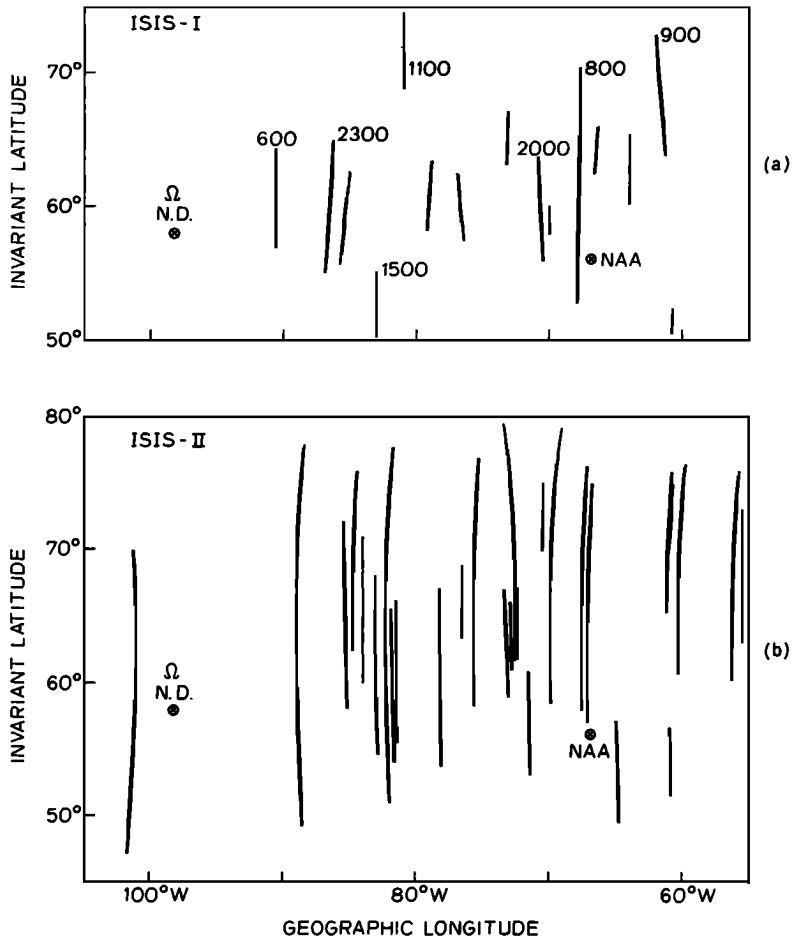

Fig. 16. Spatial distribution of spectral broadening events as observed on the ISIS 1 and 2 satellites. Location of the Omega North Dakota (Ω) and NAA transmitters are indicated by circled crosses. Numbers near the ISIS 1 tracks indicate the approximate altitude of the spacecraft during the events. Tracks not labeled lay in the 2500-to-3000-km range.

well as in signals from other VLF transmitters that happened to be present in the spectrum. These transmitters included NLK (18.6 kHz), Rugby, England (15 kHz), and the Omega transmitter in Aldra, Norway. Thus close proximity to a particular transmitter location was not a prime requisite for spectral broadening to occur in the signals from that transmitter.

For the most part the data reported here was obtained during the periods August 1979 and October-December 1980 when the local time at the ISIS 2 satellite lay in one of the two ranges: 0100-0600 LT and 1300-1800 LT. During this four-month period the spectral broadening effect was observed to occur during 27 passes out of a total of ~250, an occurrence rate of ~10%. The number of passes in each time sector was roughly equal, but, with a single exception, the effect occurred only in the 0100-0600 LT sector. Thus the occurrence rate in this sector was ~20%.

The absence of events on the dayside occurred for the most part because signals from VLF transmitters were rarely present in the data. Their absence is attributed to heavy dayside D-region absorption.

Most spectral broadening events occurred during conditions of low to moderate geomagnetic activity. This circumstance is illustrated in Figure 17 where each column of the solid-line graph gives the percentage of cases of spectral broadening for which the planetary geomagnetic index Kp lay in the range $(m-1) \leq Kp \leq m-$, where $m = 1, \cdots, 6$. It can be seen from the figure that over one-half of the events occurred during quiet conditions for which $Kp \leq 2-$ and that most of the remaining events occurred during conditions of moderate disturbance in which $2 \leq Kp \leq 4-$.

Also shown in Figure 17 (in dashed line) is the Kp distribution for all those three-hourly Kp intervals that fell within the 0100-0600 LT operations sector during the entire four-month operation period. Comparison of the two curves shows that the spectral broadening events tended to occur during the quieter periods during the campaign.

3. Discussion

In the above we have documented the main characteristics of the spectral broadening of VLF

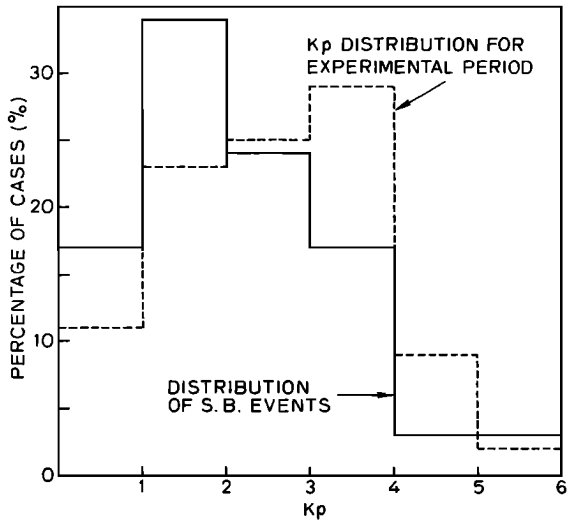

Fig. 17. Distribution of spectral broadening events as a function of the planetary geomagnetic index Kp (solid line). Shown in dashed line is the Kp distribution for all 3 hourly Kp intervals that fell within the 0100-0600 LT sector during the entire 4-month operating period.

transmitter signals during transionospheric propagation. Below we discuss some of the possible ramifications of these characteristics.

3.1. Precipitating Particles

We have shown that spectral broadening occurs only in the presence of impulsive VLF hiss and/or the presence of an irregular LHR noise band. In the past, both impulsive VLF hiss and irregular LHR noise bands have been linked to the precipitation of low-energy (<1 keV) electrons [McEwen and Barrington, 1967; Laaspere et al., 1971; Barrington et al., 1971] and direct verification has been obtained of the association between auroral zone VLF hiss and intense fluxes of low-energy electrons in the range $100 \leq E \leq 2$ keV. In fact, a strong correlation was found between precipitating electrons with energy near 700 eV and auroral hiss forms very similar to the V-shaped hiss form and the irregular LHR noise band shown in the lower panel of Figure 3 [Gurnett and Frank, 1972; Hoffman and Laaspere, 1972; Laaspere and Hoffman, 1976].

In view of this situation it can be speculated that the precipitating electrons provide the means by which spectral broadening occurs, not only in the case shown in Figure 3 but in all cases in which spectral broadening is observed. Unfortunately, no direct test of this hypothesis can be made since the ISIS 1 and 2 energetic particle detectors were not operational in 1979 and 1980, and the ISEE 1 particle detectors were inactive during the ISEE 1 events. Nevertheless, if precipitating electrons drive the spectral broadening mechanism, then the occurrence pattern of the spectral broadening events should agree roughly with the occurrence pattern of energetic electron precipitation as established by other experiments.

It can be shown from Figure 16 that the average invariant latitude at which spectral broadening was observed was 65°. This value is approximately equal to the low-latitude boundary of the nightside visual auroral zone. It lies in the middle of the particular nightside low-energy electron precipitation zone measure by the Aurora and OGO 4 satellites and designated the 'auroral' electron precipitation zone by Burch [1968] and the 'band' precipitation zone by Hoffman [1969].

On the other hand, many of the spectral broadening events extend below 60° invariant in a region where the fluxes of precipitating low-energy electrons are much less intense than in the region poleward [Gurnett and Frank, 1972]. However, these lower fluxes may still exceed whatever threshold value exists for the production of the spectral broadening effect.

3.2. Association With Impulsive ELF Hiss

In the above we have demonstrated the association of the spectral broadening effect with a band of ELF hiss that (1) is impulsive in nature, (2) lies below 700 Hz in frequency, (3) exhibits an upper cutoff frequency that depends strongly upon the spacecraft dipole antenna orientation, and (4) is seen in association with impulsive VLF hiss and irregular LHR noise bands.

To our knowledge, ELF hiss of this nature has not previously been discussed in the literature although spectrograms of hiss that may be related have been published (e.g., see Figures 5 and 6 of Rodriguez and Gurnett [1971]). The hiss appears to always lie below the local proton gyrofrequency and the local proton-helium two-ion-cutoff frequency [Gurnett and Burns, 1968] and thus may consist of electromagnetic waves polarized in either the right- or left-hand sense [Gurnett et al., 1965]. However, the variation of the upper-cutoff frequency of this noise band with antenna orientation suggests that it may be electrostatic in nature.

The impulsive ELF hiss does not appear to be related to the two other natural noise bands known as 'polar chorus' and 'plasmaspheric hiss,' which have been observed in similar frequency ranges. Polar chorus tends to occur predominantly at high latitudes and in the daytime and often has a high degree of structure [Ungstrup and Jackerott, 1963]. The impulsive ELF hiss, on the other hand, is relatively unstructured in the frequency domain and was observed predominantly at nighttime. Plasmaspheric hiss tends to be confined predominantly within the plasmasphere [Thorne et al., 1973], while the impulsive ELF hiss was observed to be much higher in amplitude outside the plasmasphere.

Efforts to detect the ELF hiss band in data acquired on the ground at Roberval Station in Canada, close to the subsatellite point, have proved fruitless, largely due to the effect of intense man-made interference lines in the ELF band at harmonics of 60 Hz. However, if the impulsive ELF hiss is truly electrostatic in nature, detection at ground stations would generally not be possible.

We have shown that at any given time the bandwidth of the impulsive ELF hiss is generally roughly one-half of the bandwidth of the spec-

trally broadened transmitter pulses. At first sight this association between the ELF hiss and the spectrally broadened pulses might suggest that the spectral broadening occurs because of harmonic distortion in the satellite receivers which results from second-order inter-modulation of the ELF hiss and the VLF transmitter pulses. However, this possibility can be ruled out on the basis of other characteristics of the effect, such as its chevron form and its occurrence only at frequencies above the local LHR frequency. Thus our physical picture provides a consistent interpretation of the observations in a way that precludes instrumental effects.

3.3. Doppler Shift Model

The spectral broadening of transmitter pulses can be interpreted as caused by the Doppler effect. If we assume that each pulse consists of a set of components at the same frequency, but with different wave vectors, the Doppler-shifted signal seen on the spacecraft could exhibit significant spectral broadening about the nominal signal frequency, if the magnitude and direction of the wave vectors is appropriate.

Amplitude scans such as those shown in Figures 10 and 11 give the power spectrum of the spectrally broadened pulses as a function of frequency near the carrier. If the sideband components actually arise from a Doppler shift effect, then information concerning the wave vectors $\vec{k}$ of the sideband components can be obtained by transforming the power spectrum into a Poynting flux spectrum that depends only on wave normal direction. This transformation is carried out in the appendix, where it is shown that wave components with $\vec{k}$ vectors near the magnetic meridian plane could be responsible for the observed large bandwidths (>100 Hz) of the transmitter signals. The calculations of the appendix also establish that most of the wave energy would be carried by waves with wave vectors within a few degrees of the resonance cone and with moderate to high values of the refractive index.

In the Doppler shift model, the fact that the spectrally broadened pulses have a spectrum with a characteristic chevron form (see Figure 9) is interpreted as implying that the sideband components of the received signal have propagated from some altitude well below the spacecraft and that increasingly larger group delays are associated with spectral components at increasingly larger apparent frequency shifts from the carrier. Thus the frequency-time dispersion can be taken as a measure of the distance that the VLF waves propagated from the apparent source region. This relative dispersion can be quite large; e.g., in the case shown in Figure 9, the maximum dispersion is approximately 100 ms, a value approximately the same as the total delay of the carrier signals to the spacecraft.

In the Doppler shift model the apparent frequency shift of any sideband component has the value $\Delta\omega = \vec{k} \cdot \vec{V}$, where k is the wave vector and $\vec{V}$ is the satellite velocity vector. Since the real frequency of each sideband component is the same as the carrier, the dispersion in each pulse is due entirely to the spread in group velocity among the sidebands, which results from the spread in $\vec{k}$.

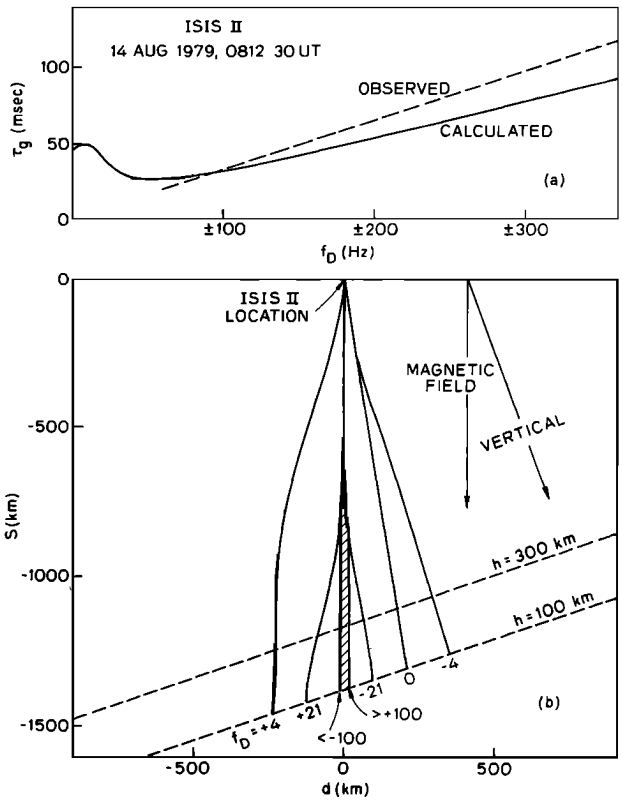

Fig. 18. Ray tracing results: (a) Calculated group delay of sideband components shown as a function of Doppler shift. Measured delay is indicated by the dashed line. Sideband components are assumed to propagate to the satellite from 100-km altitude. (b) Rays originating near the E region and reaching the satellite location. Indicated values of Doppler shift (f_D) are those that would be measured on the satellite. The hatched area represents the region that contains all ray paths for which $|f_D| > 100$ Hz.

By using the data acquired on August 14, 1979 (see Figure 7), the chevron form has been quantitatively investigated by tracing rays in two dimensions in the time-reversed sense from the height of the spacecraft toward the peak of the F region. A horizontally stratified electron density model was based on topside sounder ionograms recorded in the same area a day previously. The electron plasma frequency at the spacecraft was 0.5 MHz, $f_oF_2 = 5.0$ MHz and $h_mF_2 = 300$ km. The magnetic field lines were approximated as straight lines and the magnitude of the magnetic intensity was assumed to vary as the cube of geocentric distance.

The final wave vectors at the spacecraft were constrained to lie in the magnetic meridional plane, and to correspond to the observed sideband separations, requiring refractive indices of up to 1000. The dispersion relation for the whistler mode in a cold plasma composed of electrons and one type of ion was used. The high indices of refraction corresponding to quasi-electrostatic k vectors near the resonance cone are supplied by this theory.

Rays originating near the E region and reach-

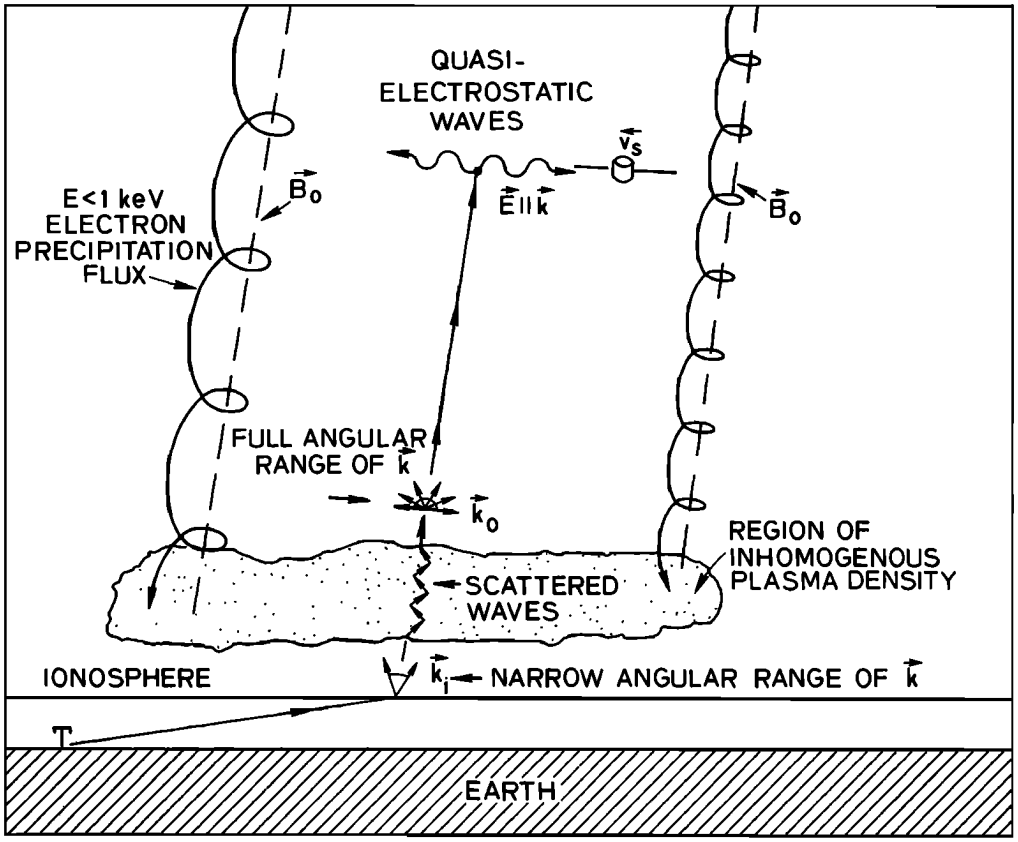

Fig. 19. Schematic of linear scattering mechanism in which transmitter pulses scatter coherently from field-aligned electron density irregularities produced by precipitating energetic electrons below 1 keV.

ing the satellite location at 1400 km are shown in Figure 18b. In tracing these rays, a cold $0^+ - e^-$ plasma was assumed. The rays chosen for display correspond to the indicated values of f_D (Doppler shift) around $f_0 = 13.1$ kHz, where f_D represents the Doppler shift that would be observed at the ISIS 2 location. The hatched area represents the region which contains all rays for which $|f_D| > 100$ Hz. It is clear that waves with $|f_D| > 100$ Hz are constrained to almost exactly the same ray paths, and these ray paths 'sample' a very narrow cone of space about the magnetic field lines.

Hence, it seems reasonable to postulate that at every instant the satellite sees a localized apparent source region for all the waves with $|f_D| > 100$ Hz. Each region could give rise to a clean chevron shape. The top panel of Figure 18 shows the calculated dispersion in group-delay versus Doppler-shift for rays terminating at 100 km altitude. Rays stopped at 300 km altitude (not shown) have ~10 ms less group delay across the entire f_D band. It is found that the observed slope is ~20% greater than the calculated one; thus reasonable agreement exists between theory and observation.

The calculations show that the rays with $50 < |f_D| < 300$ Hz retain high wave normal angles and high refractive indices throughout their paths. Such rays might be subject to guiding in density depletion ducts but, if so, their paths would be essentially the same [Helliwell, 1965].

Raytracing tests with a hot plasma theory assuming infinitely massive ions were also carried out. These indicated that the cold plasma theory behind Figure 18 is sufficiently accurate for present raytracing purposes. Furthermore, the use of finite mass ions in the hot plasma theory would not change the essential characteristics of the resonance cones and the associated group velocities that are under consideration here [Muldrew and Estabrooks, 1969].

These ray optics results suggest that if the Doppler effect is the cause of the broadening in the transmitter pulses of August 14, 1979, the apparent source of the sideband components of the pulse must be located close to the F region peak or below it. This deduction appears equally valid whatever may be the mechanism for producing the large spread in wave vectors in the components of the pulse.

3.4. Linear Scattering Source Mechanism

A mechanism for producing a large spread in the wave vectors of transmitter pulses at low altitudes is illustrated in Figure 19. Precipitating, low-energy (E < 1 keV) electrons create quasi-stationary field-aligned plasma density irregularities in the 200-to-300 km altitude range. VLF transmitter signals entering the region of precipitation from the lower iono-

sphere scatter coherently from the irregularities and the scattered wave spectrum has components whose wave normals are near the resonance cone (assuming $f > f_{LHR}$). The slow (200 km/s) quasi-electrostatic mode waves near the resonance cone have $\vec{k} \| \vec{E}_w$, where $\vec{k}$ is within a few degrees of the perpendicular to the earth's magnetic field $\vec{B}_o$.

The motion of the satellite produces a large Doppler shift in the electrostatic wave components, resulting in a greatly broadened spectrum for the signals. Since the short-wavelength quasi-electrostatic mode exists only for $f > f_{LHR}$ [Stix, 1962], scattered components of pulses for which $f < f_{LHR}$ cannot achieve a high refractive index and will be observed with very little Doppler shift. This situation would be in keeping with the observations that showed that only signals with $f > f_{LHR}$ exhibited spectral broadening.

As an example of this effect consider the case of the spectral broadening observed after 0917:40 UT on November 5, 1980, and illustrated in Figure 5. In this case the maximum bandwidth of pulses within the LHR noise band was approximately 800 Hz, corresponding to maximum Doppler shifts of ±400 Hz. Using the usual Doppler shift relation, we then have $400 \text{ Hz} = |\vec{k} \cdot \vec{v}|/2\pi$, where $\vec{k}$ is the wave vector and $\vec{v}$ is the satellite velocity vector. The minimum value of refractive index n_m, which satisfies this relation, is obtained when $\vec{k}$ and $\vec{v}$ are parallel. Using $V = 7$ km/s and $f = 13.1$ kHz, we find $n_m = 1300$. This value of refractive index gives a wave phase velocity of 230 km/s, which is comparable to the thermal electron velocity of 200 km/s and much larger than the ion thermal velocity of ~4 km/s. The wave length of this component would be approximately 18 m, a much smaller value than the 75-meter dipole antenna on the ISIS 2 spacecraft.

Up until 0918:03 UT on November 5, all pulses at 10.2 kHz lay below the LHR frequency and showed little evidence of spectral broadening. The average value of the lower cutoff frequency of the LHR noiseband during this time was approximately 11.5 kHz. Using this value as the local LHR frequency, we can find the maximum value of the refractive index at 10.2 kHz from the well-known relation:

$$n = \left[\frac{RL}{s}\right]^{1/2} \qquad (1)$$

where $s = \frac{1}{2}[R+L]$

and

$$R = R(\epsilon_\kappa) = 1 - \sum_\kappa \frac{\omega_\kappa^2}{\omega^2}\left(\frac{\omega}{\omega + \epsilon_\kappa \omega_{H\kappa}}\right)$$

$$L = L(\epsilon_\kappa) = R(-\epsilon_\kappa)$$

where the index κ is used to denote the κ^{th} type of ionized particle, ω_κ and $\omega_{H\kappa}$ are the plasma frequency and gyrofrequency, respectively, of the κ^{th} type of particle and where ϵ_κ gives the sign of the charge of the κ^{th} type of particle (see Stix [1962]).

Assuming that the electron density at 1400 km had a value of $N_e \sim 3 \times 10^3/\text{cm}^3$, a common nighttime value, (1) yields $n \simeq 50$. This value of n gives a maximum Doppler shift of approximately 12 Hz. Thus, very little spectral broadening would be expected to occur at 10.2 kHz even though the waves at this frequency had been scattered strongly by the irregularities.

Since the carrier energy is being continuously scattered into components with larger wave vectors in the region of irregularities, we might expect that the sideband amplitude would eventually reach that of the carrier. Furthermore, since Figure 18 shows that waves with small Doppler shifts have much larger divergence than waves with large Doppler shifts, we might expect that the amplitude of the sideband components with high Doppler shift could often exceed that of the carrier. Thus the linear scattering mechanism may be able to explain the amplitude minimum that often occurs at the carrier frequency of the spectrally broadened pulses.

In general, Doppler shifts of the order of 400 Hz or more require wave refractive indices of more than 10^3. In this case the wave phase velocity is comparable to the ambient electron thermal velocity, and significant Landau damping of the large $\vec{k}$ components can be expected if the electron distribution function is isotropic. Thus it may be necessary to hypothesize that the presence of the precipitating energetic electrons results in an anisotropic electron distribution function which does not significantly damp the large k components as they propagate up to the satellite from the scattering region. An example of a system in which precipitating particles lead to amplification of electrostatic waves near ω_{LHR} is discussed by Horita and Watanabe [1969].

3.5. Nonlinear Scattering Mechanism

It is possible that the sideband components of the spectrally broadened signals are produced by a nonlinear scattering (mode coupling) process involving the impulsive ELF hiss and the input transmitter pulses. The well-known synchronism conditions for this type of interaction are [Barbosa, 1982]

$$\omega_i \pm \omega_s = \omega_o$$
$$\vec{k}_i \pm \vec{k}_s = \vec{k}_o \qquad (2)$$

where ω_i and $\vec{k}_i$ refer to the frequency and wave vector of the input transmitter signal, ω_s and $\vec{k}_s$ refer to an electrostatic ion mode, and ω_o and $\vec{k}_o$ refer to a sideband component of the output signal.

Normally, an interaction of an electromagnetic whistler-mode wave and an electrostatic ion wave would be inefficient because of the disparity between the k's. However, if precipitating particles heat the ambient protons and thereby raise the ion wave phase speed, k_s may reduce to within an order of magnitude of k_i, allowing a relatively efficient nonlinear interaction. This would be enhanced further if k_i is a quasi-electrostatic whistler-mode wave resulting from previous scattering from irregularities. The resulting quasi-electrostatic whistler-mode wave has a $\vec{k}_o$ that,

again, is near the resonance cone and has a frequency that is shifted by ω_s. The spectral broadening could be significantly greater than in the linear scattering case, in that the frequency shift of the carrier is added to the Doppler shift observed on the moving spacecraft.

A somewhat analogous mode coupling interaction has been discussed recently by Barbosa [1982] in connection with the generation of VLF and LF emissions in the magnetosphere by scattering upper hybrid waves from electrostatic ion waves. However, the results of that theory do not apply directly to the case considered here.

If the impulsive ELF hiss band is actually driven by the precipitating electrons than it is possible that nonlinear stages of beam instabilities of the precipitating electrons can also distort the transmitted pulse spectrum. For instance, in the regions of precipitation the Fourier components of the perturbed distribution function $f_1(\vec{v}, \vec{r}, t)$ of primary energetic electrons will depend upon the amplitude of the ELF wave components.

When a transmitter pulse is present in the precipitation region, initially small nonlinear terms in the Vlasov equation involving the product of velocity space derivatives of f_1 with wave quantities will produce harmonic distortion in the new perturbed distribution function. If these small terms can be amplified through a plasma instability the resulting spectral broadening could conceivably take the form reported here.

3.6. Antenna Orientation Dependence

As we have demonstrated above, in the ISIS data the bandwidth of the spectrally broadened pulses as well as that of the impulsive VLF hiss often shows a strong dependence upon the orientation of the spacecraft dipole antenna. This effect could conceivably be related to the response of the dipole to short wavelength electrostatic waves. However, this conjecture is difficult to evaluate since no widely accepted theory exists that describes the response of an electrically long dipole antenna in a magnetoplasma. Nevertheless, it should be noted here that there is some evidence that suggests that the dependence of pulse bandwidth upon antenna orientation may not be directly related to the mechanism that produces the spectral broadening of the pulses.

For instance, Gurnett et al. [1969] have reported observations from the INJUN 5 satellite in which the lower cutoff frequency of the LHR noise band was seen to be a periodic function of the orientation of the spacecraft electric dipole antenna. The lower cutoff frequency varied sinusoidally between the approximate limits 8 ± 1 kHz, while the satellite moved at an altitude of approximately 2500 km between the invariant latitude 46°-38°. A similar effect has been seen occasionally in ISIS 1 data.

This effect may be similar to that which produces the bandwidth variation of the spectrally broadened signals and may be independent of the mechanism which produces the broadening.

3.7. LHR Breakup

In Figure 3b an arrow on the time axis indicates the time at which the lower cutoff frequency of the LHR noise band becomes very irregular. This point is labeled 'LHR breakup' since it resembles the LHR noise band breakup discussed by Carpenter et al. [1968], which takes place near the plasmapause. In general, however, there are significant differences between the LHR irregularities reported by Carpenter et al. [1968] and those which are associated with the spectral broadening effect. First of all, the LHR irregularities associated with the spectral broadening effect are seen over a wide latitude range, while the classic LHR breakup effect is confined to the region near the plasmapause boundary. Furthermore, at the times of initiation of the spectral broadening effect, the lower cutoff frequency of the LHR noise band shows an abrupt increase, while in the classic LHR breakup effect it shows an abrupt decrease.

These differences suggest that the two effects are not caused by the same mechanism.

3.8. Comparison With Past Work

It is important to compare in detail the spectral broadening effect reported here and the Doppler broadening effect reported by other workers [Walter, 1965; Cerisier, 1974; Edgar, 1976]. The most striking difference between the two effects lies in the fact that the spectral broadening effect occurs in transmitter signals that have propagated over a relatively short distance between the ground and the satellite, while the Doppler broadening effect occurs in transmitter signals that have made at least one complete traversal of the magnetosphere. Furthermore, the magnitude of the two types of broadening are quite different, with bandwidths of 500 Hz being very common for spectrally broadened signals, while bandwidths greater than 250 Hz are very uncommon in the Doppler broadening phenomenon. There are, however, a number of interesting similarities:

1. Doppler broadening occurs only for wave frequencies which lie above the local LHR frequency.
2. Doppler broadened waves generally exhibit a partial chevron form and occasionally a symmetric chevron form [Edgar, 1976b, Figure 1].
3. The bandwidth of Doppler broadened waves can show a dependence upon the satellite dipole antenna orientation [Edgar, 1976b, Figure 4].
4. The 'sideband' components of the Doppler broadened waves can be of higher amplitude than the carrier.

Furthermore, the basic interpretation of the Doppler broadening effect is similar to that which we have given for the spectral broadening effect, i.e., a series of constant-frequency wave components with $\vec{k}$ vectors near the resonance cone are received on a moving satellite with a large Doppler shift, and a temporal dispersion produced by the range in $\vec{k}$ of the components.

However, an important difference is that the spread in $\vec{k}$ in the Doppler broadening effect is the result of multi-path interhemisphere wave propagation, while in our model of the spectral broadening effect the spread in $\vec{k}$ is the result of low-altitude coherent scattering by ionospheric irregularities produced by particle precipitation.

In spite of the many similarities of the spec-

tral broadening and Doppler broadening effects, it is generally not difficult to distinguish the two effects.

3.9. Particle Precipitation Experiments

If the spectral broadening effect is driven by precipitating energetic electrons, it could have important consequences for VLF wave-injection experiments designed to cause precipitation of energetic electrons from whistler-mode ducts [Inan et al., 1978; Bell et al., 1981a]. The efficiency of these experiments is much higher when the input wave is amplified by the whistler-mode instability before the particle scattering begins. However, since the precipitating particles enter the ionosphere above the wave injection point, the precipitation could actuate the spectral broadening effect, which would then markedly increase the k bandwidth of the input wave.

To a moving electron, through the Doppler shift effect, the spread in k values in the input wave would be equivalent to a spread in frequency bandwidth of the wave. From the results of past experiments [Raghuram et al., 1977] on the whistler-mode instability, there is good reason to believe that the increase in apparent bandwidth of the signal would result in a sharp decrease in the whistler-mode gain. The resultant weaker signal would produce a smaller precipitation flux, setting up a type of feedback loop. Assuming that the particle scattering takes place near the magnetic equatorial plane, the time constant of the oscillation in this loop would be $\tau \approx t_g + t_p$, where t_g is the wave group delay time in the duct from the ionosphere to the magnetic equator and t_p is the scattered particle travel time from the magnetic equator to the ionosphere. In general, $1 \leq \tau \leq 6$ s, depending upon the duct location and the energy of the scattered particles.

3.10. Downward Propagating Signals

This article has focused on the properties of transmitter signals in the northern hemisphere that display significant spectral broadening when propagating upward to spacecraft through regions of impulsive VLF and ELF hiss and irregular LHR bands. A small amount of data gathered to date indicates that similar spectral broadening effects may occasionally occur in signals propagating downward to a low-altitude satellite, either as transmissions from the opposite hemisphere (1^- mode) or as two-hop echoes of signals from transmitters in the same hemisphere (2^- mode) If this effect can be reliably distinguished from the Doppler broadening effect, the data should further clarify the physics of the VLF phenomena described herein.

4. Summary and Conclusions

We have presented evidence of the existence of a new phenomenon in which initially narrowband (~1 Hz) upgoing signals from ground-based VLF transmitters undergo a significant apparent spectral broadening as they propagate through the ionosphere and protonosphere up to altitudes in the 600-to-300 km range. The effected signals lie in the 10-to-20 kHz range and the spectral broadening can reach a value as high as 10% of the nominal carrier frequency of the input signal. We have given the conditions under which the effect occurs and have shown how the orientation of the satellite electric dipole antenna affects the bandwidth of the spectrally broadened signal. Because of the temporal dispersion in the components of the broadened pulses we have concluded that these pulses consist of components of the same frequency but with widely different wave normals that have an apparent source region near or below the F region peak.

The increased signal bandwidth is hypothesized to be produced by the large Doppler shift, observed on the moving satellite, of pulse components with wave normals near the resonance cone.

We conclude that a likely mechanism for producing the wide range of wave normals necessary for the Doppler shift model is a process in which input signals scatter coherently from magnetic field-aligned density irregularities in the 200-to-300 km altitude range. It is hypothesized that these irregularities are produced by precipitating electrons of energy less than 1 keV. Other mechanisms for producing the spectral broadening are also considered. We conclude that the spectral broadening effect represents a new type of ionospheric wave-particle interaction that may have significant implications for VLF wave-injection experiments designed to produce precipitation of energetic electrons from whistler-mode ducts.

Appendix: Spectral Transformation and Power Spectra

The quantity measured by the ISIS VLF receiver and plotted in Figures 10 and 11 is the power spectrum P_D with respect to the difference frequency f_D. The purpose of this section is to describe how it is transformed to the Poynting power spectrum P_θ with respect to the polar angle θ_k of the wave vector, assuming that Δf_D actually represents the Doppler shift f_D of each sideband component.

The quantity P_D is proportional to the square of the receiving antenna terminal voltage V. That is

$$P_D = C \cdot dV^2/df_D \tag{A1}$$

The power in a Doppler frequency range df_D about f_D is $P_D df_D$. It is assumed that this power corresponds to a dV^2 produced by an effective electric field E such that

$$dV^2 = \left(\vec{E} \cdot \vec{L}\right)^2 \tag{A2}$$

in which $\vec{L}$ is the antenna length vector with modulus L and direction cosines β_x, β_y, β_z. This power increment corresponds to the incremental Poynting power $d|\vec{s}|$ in the angular increment $d\theta_k$ about θ_k, $P\theta d\theta_k$. That is,

$$d|\vec{s}| = P\theta d\theta_k \tag{A3}$$

In what follows, P_θ is developed as a function of P_D.

According to Allis et al. [1963], the E vector components for the coordinate system in Fig-

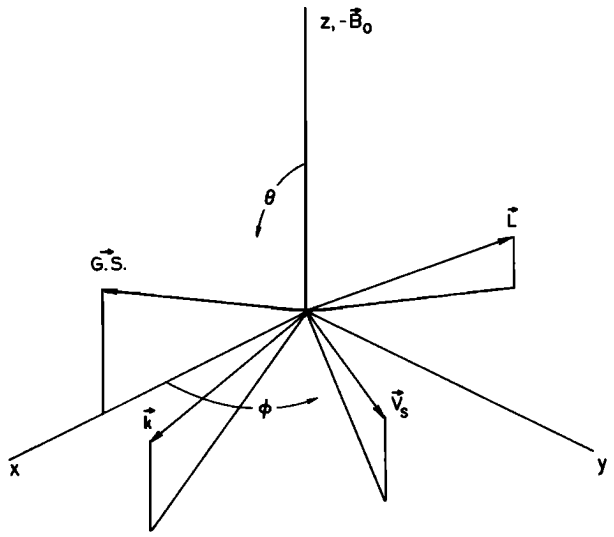

Fig. A1. Vectors used in analysis.

ure A1 are related to the E vector modulus E_o in a cold collisionless plasma as follows:

$$\left.\begin{aligned} E_x &= E_o[n^2 - K_\perp][n^2\sin^2\theta_K - K_\parallel] \equiv E_o\gamma_x \\ E_y &= iE_oK_x[n^2\sin^2\theta_K - K_\parallel] \equiv iE_o\gamma_y \\ E_z &= E_on^2\sin\theta_K\cos\theta_K[n^2 - K_\perp] \equiv E_o\gamma_z \end{aligned}\right\} \quad (A4)$$

Here, n^2 is the square of the refractive index, $K_\perp$, $K_\parallel$, and K_x are components of the dielectric tensor in the notation of Allis et al. [1963], and γ_x, γ_y, and γ_z are the direction cosines of $\vec{E}$.

With this notation and with due regard for the phase relations in (A4), expression (A2) is

$$\begin{aligned} dV^2 &= E_o^2L^2[(\gamma_x\beta_x + \gamma_z\beta_z)^2 + (\gamma_y\beta_y)^2] \\ dV^2 &= E_o^2L^2F_D \end{aligned} \quad (A5)$$

The Poynting flux is evaluated as usual as

$$d|s| = \tfrac{1}{2}|R_e(\vec{E}\times\vec{H}^*)| \quad (A6)$$

$\vec{H}^*$ being the complex conjugate of the wave magnetic field intensity vector. From Faraday's law, $\vec{\nabla}\times\vec{E} = -\mu_o(\partial H/\partial t)$, it is found with $k_y = 0$ that

$$\left.\begin{aligned} H_x^* &= nE_y\cos\theta_k/Z_o \\ H_y^* &= n(E_x\cos\theta_k - E_z\sin\theta_k)/Z_o \\ H_z^* &= -n(E_y\sin\theta_k)Z_o \end{aligned}\right\} \quad (A7)$$

where Z_o is the free space wave impedance.

With the explicit forms if (A4) and (A7), (A6) becomes

$$\begin{aligned} d|\vec{s}| = \frac{nE_o^2}{2Z_o}\Big[&(\gamma_y^2\sin\theta_k + \gamma_z^2\sin\theta_k \\ &- \gamma_z\gamma_x\cos\theta_k)^2 \\ &+ (\gamma_y^2\cos\theta_k + \gamma_x^2\cos\theta_k \\ &- \gamma_x\gamma_z\sin\theta_k)^2\Big]^{\frac{1}{2}} \end{aligned} \quad (A8)$$

$$d|\vec{s}| \equiv \frac{nE_o^2}{2Z_o}\cdot F_\theta$$

Now (A1) and (A3), respectively, can be written as

$$C\,E_o^2L^2F_D = P_D df_D \quad (A9)$$

$$\frac{nE_o^2}{2Z_o}\cdot F_\theta = P_\theta d\theta_k \quad (A10)$$

which, combined to eliminate E_o^2, yield

$$P_\theta = \left[\frac{1}{2C\,L^2\,Z_o}\right]\cdot\left[\frac{nF_\theta}{F_D}\cdot\frac{df_D}{d\theta_k}\cdot P_D\right] \quad (A11)$$

The Doppler frequency f_D at a receiver in a spacecraft with velocity $\vec{V}_s$ is $f_D = -\vec{V}_s\cdot\vec{k}/2\pi$. The derivative of f_D in (A11) has been evaluated by using

$$\begin{aligned} \frac{df_D}{d\theta_k} = |\vec{V}_s|k\Big[&\eta_x\tan\alpha\sin\theta_k - \eta_x\cos\theta_k \\ &+ \eta_z\tan\alpha\cos\theta_k \\ &+ \eta_z\sin\theta_k\Big] \end{aligned} \quad (A12)$$

where η_x, η_y, and η_z are the direction cosines of $\vec{V}_s$, and $dk/d\theta_k$ has been replaced by $-k$ times the tangent of the angle between the group velocity and $\vec{k}$ directions.

Examples of wave power spectra, including those in Figure 11, have been converted to (differential) Poynting flux P_θ with respect to wave vector directions using the relations given above. In these calculations only the form of the P_θ curves was determined, and no attempt was made to calculate the absolute P_θ. Thus, in (A11), the quantities inside the second set of brackets were evaluated while those inside the first have been disregarded.

The spatial relationship among important vectors is shown in Figure A1. The xyz coordinate system has z along the direction of the terrestrial magnetic field $\vec{B}_o$. The geographic south direction $\vec{GS}$ lies in the xz plane. In our ISIS data set, the spacecraft velocity vector $\vec{V}_s$ is close to $\pm\vec{GS}$, while the receiving dipole vector $\vec{L}$ executes spin motion that carries it within a few degrees of the z and x axes. The test $\vec{k}$ vectors all lie in a plane at some azimuth ϕ_k passing through the z axis. The goal of the calculation is to compute the distribution of power with respect to θ_k (wave-vector polar angle) for various values of the azimuth ϕ_k. The L direction was computed from real-time magnetometer and sun sensor data, $\vec{B}_o$ was based on a real-field model and $\vec{GS}$ and $\vec{V}_s$ were computed from spacecraft ephemeris data.

The observed power spectral density P_D commonly exhibits a notch near the nominal transmitter frequency. Therefore, empirical fits to

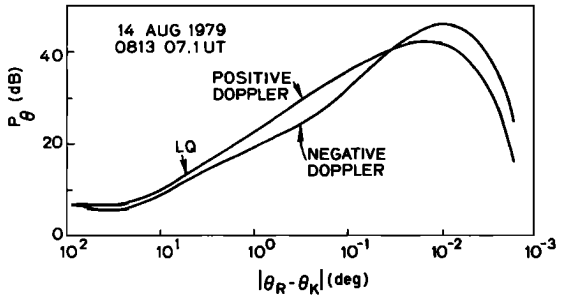

Fig. A2. Theoretical differential Poynting power spectrum with respect to the difference between the wave vector angle θ_k and the resonance cone angle θ_R. The wave normals are assumed to lie in the magnetic meridional plane.

the observations could in many cases be found by using the difference of two Gaussian distributions:

$$P_D = I_1 \exp(-f_\varepsilon^2/w_1^2) = I_2 \exp(-f_\varepsilon^2/w_2^2) \quad (A13)$$

where $f_\varepsilon \equiv f - f_c - \varepsilon$, f_c is the nominal carrier frequency, ε is the frequency offset of the notch in P_D from f_c, and I_1, I_2, w_1, and w_2 are constants chosen to produce the best fit. For illustration, a fitted analytical curve is superposed on the data in Figure 11e in dashed line. For this case the parameters have the values $I_1 = 1$, $I_2 = 0.93$, $w_1 = 100$ Hz, $w_2 = 60$ Hz, and $\varepsilon = 20$ Hz. The P_θ curve for this example is shown in Figure A2, where P_θ is plotted as a function of the difference between the wave vector angle θ_k and the resonance cone angle θ_R. In preparing the figure it was assumed that $\phi_k = 0$.

Generally, P_θ increases with decreasing $\theta_R - \theta_k$. Its peak moves to larger $\theta_R - \theta_k$ as the widths w_1 and w_2 increase.

Figure A2 gives the impression that most of the wave power flux is concentrated near the resonance cone. This is confirmed by integrating P_θ. As a measure of the power concentration, the lower quartile point

$$\int_0^{\theta'} P_\theta d\theta \Big/ \int_0^{\theta_R} P_\theta d\theta = 0.25$$

was solved for θ'. The result invariably placed θ' within a few degrees of θ_R (see 'L.Q.' arrows in Figure A2). Thus most of the detected radiation corresponds to k vectors lying close to the resonance cone with indices of refraction of ~20 or greater.

Tests were made by varying the azimuth of the k vector distribution θ_k. When the azimuth of the k-plane lay within approximately ±45° of the $\vec{GS}$-$\vec{B}_0$ plane, the computed P_θ shape did not change significantly.

For cases with the $\vec{k}$ azimuth more nearly perpendicular to $\vec{GS}$, and therefore to $\vec{V}_s$, ($\phi_k \simeq 90$) increasingly larger refractive indices n were required to produce the observed frequency shifts. The hot plasma dispersion relations for the whistler mode [Muldrew and Estabrooks, 1969] admit solutions for n values up to about 1000, beyond which propagation is thermally damped. Here an arbitrary upper limit of n = 1000 provided the cutoff on the right side of the curves in Figure A2.

Distributions with $60° < \phi_k < 120°$ were found incapable of producing the observed wings of the P_D distributions. It was concluded that the real wave vector distributions have strong components near the geographic south and north directions. Nothing can be deduced about the existence of waves with $\vec{k}$'s oriented roughly east and west.

Acknowledgments. The authors acknowledge valuable discussions with D. L. Carpenter and R. A. Helliwell, and J. Yarbrough concerning the data discussed herein. The continuing support in ISIS scheduling and data acquisition by the Satellite Controller and his staff at Communications Research Centre, Ottawa, is deeply appreciated. The work of the three authors (TFB, USI, and JPK) was supported by the National Aeronautics and Space Administration under contracts NAS5-20871 and NGL-05-020-008. The work of the remaining author was supported by the Canadian Government through the Communications Research Centre. The spectrograms shown in this paper were produced by J. Yarbrough, and the text was prepared by K. Faes and K. Dean.

The Editor thanks R. L. Dowden and R. R. Anderson for their assistance in evaluating this paper.

References

Allis, W. B., S. J. Buchsbaum, and A. Bers, Waves in Anisotropic Plasmas, MIT Press, Cambridge, Mass., 1963.

Angerami, J. J., and J. O. Thomas, Studies of planetary atmospheres, 1, The distribution of electrons and ions in the earth's exosphere, J. Geophys. Res., 69, 4537, 1964.

Barbosa, D. D., Low-level VLF and LF radio emissions observed at earth and Jupiter, Rev. Geophys. Space Phys., 20, 316, 1982.

Barrington, R. E., J. S. Belrose, and G. L. Nelms, Ion composition and temperature at 1000 km as deduced from simultaneous observations of a VLF plasma resonance and topside sounding data from the Alouette I satellite, J. Geophys. Res., 70, 1647, 1965.

Barrington, R. E., T. R. Hartz, and R. W. Harvey, Diurnal distribution of ELF, VLF, and LF noise at high latitudes as observed by Alouette, J. Geophys. Res., 76, 5278, 1971.

Bell, T. F., and R. A. Helliwell, The Stanford University VLF wave injection experiment on the ISEE-A spacecraft, IEEE Trans. Geosci. Electron., GE-16, 248, 1978.

Bell, T. F., U. S. Inan, and R. A. Helliwell, Nonducted coherent VLF waves and associated triggered emissions observed on the ISEE 1 satellite, J. Geophys. Res., 86, 4649, 1981a.

Bell, T. F., and U. S. Inan, Doppler shift of VLF waves injected into the magnetosphere

from Siple Station, EOS, 62, 991, 1981b.
Bell, T. F., H. G. James, U. S. Inan, and J. P. Katsufrakis, The spectral broadening of VLF transmitter signals during transionospheric propagation, EOS, 63, 401, 1982.
Bruene, W. B., MSK simplified, Monogr. WP-9262, Collins Radio Company, Dallas, Texas, 1971.
Burch, J. L., Low-energy electron fluxes at latitudes above the auroral zone, J. Geophys. Res., 73, 3583, 1968.
Carpenter, D. L., Whistler studies of the plasmapause in the magnetosphere, 1, Temporal variations in the position of the knee and some evidence of plasma motions near the knee, J. Geophys. Res., 71, 693, 1966.
Carpenter, D. L., F. Walter, R. E. Barrington, and D. J. McEwen, Alouette 1 and 2 observations of abrupt changes in whistler rate and of VLF noise variations at the plasmapause — A satellite-ground study, J. Geophys. Res., 73, 2929, 1968.
Cerisier, J. C., A theoretical and experimental study of nonducted VLF waves after propagation through the magnetosphere, J. Atmos. Terr. Phys., 35, 77, 1973.
Dowden, R. L., A. C. McKey, L. E. S. Amon, H. C. Koons, and M. H. Dazey, Linear and nonlinear amplification in the magnetosphere during a 6.6-kHz transmission, J. Geophys. Res., 83, 169, 1978.
Edgar, B. C., The upper and lower frequency cutoffs of magnetospherically reflected whistlers, J. Geophys. Res., 81, 205, 1976a.
Edgar, B. C., The theory of VLF doppler signatures and their relation to magnetospheric density structure, J. Geophys. Res., 81, 3327, 1976b.
Florida, C. D., The development of a series of ionospheric satellites, Proc. IEEE, 57, 867, 1969.
Franklin, C. A., T. Nishizaki, and W. E. Mather, A wideband receiver for the Alouette-II and ISIS-A satellites, DRTE Tech. Memo. 522, Dept. of Nat. Defence, Ottawa, Canada, May, 1960.
Gurnette, D. A., and T. B. Burns, The low-frequency cutoff of ELF emissions, J. Geophys. Res., 73, 7437, 1968.
Gurnett, D. A., and L. A. Frank, VLF hiss and related plasma observations in the polar magnetosphere, J. Geophys. Res., 77, 172, 1972.
Gurnett, D. A., S. D. Shawhan, N. M. Brice, and R. L. Smith, Ion cyclotron whistlers, J. Geophys. Res., 70, 1665, 1965.
Gurnett, D. A., G. W. Pfeiffer, R. R. Anderson, S. R. Mosier, and D. P. Cauffman, Initial observations of VLF electric and magnetic fields with Injun 5 satellite, J. Geophys. Res., 74, 4631, 1969.
Helliwell, R. A., Whistlers and Related Ionospheric Phenomena, Stanford University Press, Stanford, Calif., 1965.
Helliwell, R. A., and J. P. Katsufrakis, VLF wave injection into the magnetosphere from Siple Station, Antarctica, J. Geophys. Res., 79, 2511, 1974.
Hoffman, R. A., Low-energy electron precipitation at high latitudes, J. Geophys. Res., 74, 2425, 1969.
Hoffman, R. A., and T. Laaspere, Comparison of very-low-frequency auroral hiss with precipitating low-energy electrons by the use of simultaneous data from two OGO 4 experiments, J. Geophys. Res., 77, 640, 1972.
Horita, R. E., and T. Watanabe, Electrostatic waves in the ionosphere excited around the lower hybrid resonance frequency, Planet. Space Sci., 17, 61, 1969.
Inan, U. S., T. F. Bell, and R. A. Helliwell, Nonlinear pitch angle scattering of energetic electrons by coherent VLF waves in the magnetosphere, J. Geophys. Res., 83, 3235, 1978.
Laaspere, T., and R. A. Hoffman, New results on the correlation between low-energy electrons and auroral hiss, J. Geophys. Res., 81, 524, 1976.
Laaspere, T., and H. A. Taylor, Jr., Comparison of certain VLF noise phenomena with the lower hybrid resonance frequency calculated from simultaneous ion composition measurements, J. Geophys. Res., 75, 97, 1970.
Laaspere, T., W. C. Johnson, and L. C. Semprebon, Observations of auroral hiss, LHR noise, and other phenomena in the frequency range 20 Hz-540 kHz on OGO 6, J. Geophys. Res., 76, 4477, 1971.
McEwen, D. J., and R. E. Barrington, Some characteristics of the lower hybrid resonance noise bands observed by the Alouette I satellite, Can. J. Phys., 45, 13, 1967.
McPherson, D. A., H. C. Koons, M. H. Dazey, R. L. Dowden, L. E. S. Amon, and N. R. Thomson, Conjugate magnetospheric transmissions of VLF from Alaska to New Zealand, J. Geophys. Res., 79, 1555, 1974.
Muldrew, D. B., and M. F. Estabrooks, Computation of dispersion curves for a hot magnetoplasma with application to the upper-hybrid and cyclotron frequencies, Radio Sci., 7, 579, 1969.
Raghuram, R., T. F. Bell, R. A. Helliwell, and J. P. Katsufrakis, Echo-induced suppressions of coherent VLF transmitter signals in the magnetosphere, J. Geophys. Res., 82, 2787, 1977.
Rodriguez, P., and D. A. Gurnett, An experimental study of very-low-frequency mode coupling and polarization reversal, J. Geophys. Res., 76, 960, 1971.
Smith, R. L., and N. Brice, Propagation in multicomponent plasmas, J. Geophys. Res., 69, 5029, 1964.
Stix, T. H., The Theory of Wave Plasmas, McGraw-Hill, New York, 1962.
Strangeways, H. J., and M. J. Rycroft, Trapping of whistler-waves through the side of ducts, J. Atmos. Terr. Phys., 42, 983, 1980.
Thorne, R. M., E. J. Smith, R. K. Burton, and R. E. Holzer, Plasmaspheric hiss, J. Geophys. Res., 78, 1581, 1973.
Ungstrup, E., and I. M. Jackerott, Observations of chorus below 1500 cycles per second at Godhavn, Greenland, from July 1957 to December 1961, J. Geophys. Res., 68, 2141, 1963.
Walter, F., Non-ducted VLF propagation in the magnetosphere, Tech. Rep. 3418-1, Stanford Electron. Lab., Stanford, Calif., 1965.

(Received July 29, 1982;
revised December 13, 1982;
accepted January 11, 1983.)